

**Determination of the spatial and temporal variability of size-resolved  
PM<sub>2.5</sub> composition and mixing state in multiple regions in California**

Final Report to California Air Resources Board  
Contract No. 04-336  
Prepared for the California Air Resources Board

December 1, 2009

*Principal Investigator*  
Kimberly Prather

*Contributors*  
Andrew P. Ault  
Stephen M. Toner  
Laura G. Shields  
Xueying Qin  
Kerri A. Pratt  
Jessie M. Creamean  
Margaret Yandell  
Cassandra J. Gaston  
Meagan J.K. Moore

Department of Chemistry & Biochemistry  
University of California San Diego  
9500 Gilman Drive MC 0314  
La Jolla, CA 92093-0314

## **DISCLAIMER**

The statements and conclusions in this Report are those of the contractor and not necessarily those of the California Air Resources Board. The mention of commercial products, their source, or their use in connection with material reported herein is not to be construed as actual or implied endorsement of such products.

## **ACKNOWLEDGEMENTS**

We thank the following people for their contributions to the research described in this report:

Ms. Melanie Zauscher  
Dr. Matt Spencer  
Dr. Ryan Moffet  
Dr. Ryan Sullivan  
Dr. Robert Moison  
Dr. Hiroshi Furutani  
Dr. Thomas Rebotier

and thank Drs. Eileen McCauley and William Vance (CARB) for their assistance and advice during this contract.

This Report was submitted in fulfillment of Contract No. 04-336, “Determination of the spatial and temporal variability of size-resolved PM<sub>2.5</sub> composition and mixing state in multiple regions in California” under the sponsorship of the California Air Resources Board. Work was completed as of October 13, 2009.

# TABLE OF CONTENTS

|  |       |
|--|-------|
| DISCLAIMER.....  | ii    |
| ACKNOWLEDGEMENTS .....   | iii   |
| TABLE OF CONTENTS .....  | iv    |
| LIST OF FIGURES .....  | ix    |
| LIST OF TABLES .....   | xviii |
| ABSTRACT .....   | xix   |
| EXECUTIVE SUMMARY .....  | xx    |
| Background.....  | xx    |
| Methods .....  | xx    |
| Results and Conclusions .....  | xxi   |
| Body of Report.....  | 1     |
| I. Introduction.....   | 1     |
| 1. Research Objectives and Studies Conducted .....   | 1     |
| 2. Instrumentation .....   | 2     |
| 3. Data Analysis Methods.....  | 4     |
| 4. Summary of Chapters .....   | 5     |
| i. Introduction .....  | 5     |
| ii. Time and Size Resolved Chemical Composition Measurements Detailing Short Term Changes in Composition.....  | 5     |
| iii. Spatial Variability of Particulate Matter and Sources .....   | 6     |
| iv. Seasonal and Interannual Variability in Particulate Matter Size and Composition.....   | 7     |
| v. Mass Comparisons and Investigations into the Volatile and Semivolatile Fraction of Particles .....  | 9     |
| vi. Changes in the Size-Resolved Particle Composition Linked with Meteorological Measurements and Air Mass Back Trajectories to Increase Understanding of Sources and Secondary Contributions to Particulate Matter..... | 10    |
| vii. Development of Source Apportionment Algorithms.....   | 11    |
| II. Objectives and Results.....  | 13    |
| Time and Size Resolved Chemical Composition Detailing Short Term Changes in Composition.....   | 13    |
| 1. Detection of ambient ultrafine aerosols by single particle techniques during the SOAR 2005 campaign.....  | 13    |
| i. Introduction.....   | 13    |
| ii. Experimental .....   | 14    |
| iii. Results and discussion .....  | 16    |
| a. Ambient measurements .....  | 16    |
| b. Afternoon photochemical events .....  | 23    |
| c. Seasonal differences .....  | 25    |
| d. Comparison of ultrafine particle measurements .....   | 27    |
| iv. Acknowledgements .....   | 28    |
| 2. Characterization of the Single Particle Mixing State of Individual Ship Plume Events measured at the Port of Los Angeles.....   | 29    |
| i. Introduction.....   | 29    |
| ii. Experimental .....   | 29    |
| a. Sampling Information .....  | 29    |
| b. Gas and Particle Peripheral Instrumentation .....   | 30    |
| c. Aerosol Time-of-Flight Mass Spectrometry (ATOFMS) .....   | 30    |
| d. Single Particle Analysis.....   | 30    |
| iii. Results and Discussion .....  | 30    |
| a. Ship Identification .....   | 30    |
| b. Plume Characterization .....  | 32    |
| c. In Plume Gas Phase Chemistry and Concentrations.....  | 33    |
| d. Unique Plume Chemistry .....  | 34    |
| e. Details on the OC-V-sulfate and Fresh Soot Particle Types.....  | 36    |

|  |     |
|--|-----|
| f. Description of the Ca-ECOC Particle Type .....  | 38  |
| g. Background Particle Types During Plumes .....   | 39  |
| h. Temporal Trends .....   | 41  |
| i. Size-resolved Chemistry.....  | 42  |
| j. Correlation between sulfate and vanadium particle.....  | 43  |
| iv. Acknowledgements .....   | 45  |
| Spatial Variability of Particulate Matter and Sources.....   | 46  |
| 3. <i>Mobile Laboratory Observations of Temporal and Spatial Variability within the Coastal Urban</i>  |     |
| Aerosol.....   | 46  |
| i. Introduction.....   | 46  |
| ii. Experimental .....   | 47  |
| a. Mobile ATOFMS Laboratory.....   | 47  |
| b. 2009 San Diego Bay Measurements.....  | 47  |
| c. Instrumentation .....   | 49  |
| d. Aerosol Time-of-Flight Mass Spectrometry.....   | 50  |
| e. Single Particle Data Analysis .....   | 50  |
| f. Scaling Single Particle Measurements to Mass Concentrations.....                                    | 50  |
| iii. Results and Discussion .....  | 51  |
| a. Temporal Patterns of Meteorological and Gas Phase Concentrations .....                              | 51  |
| b. Variability of Particle Mass and Number Concentrations .....  | 53  |
| c. Variation in Aerosol Size Distributions .....   | 55  |
| d. Differing Aerosol Sources Determined by Particle Chemistry.....                                     | 57  |
| e. Differences in Particle Aging and Mixing State .....  | 59  |
| f. Variations in Chemistry and Implications for Models and Regulations.....                            | 61  |
| iv. Acknowledgements .....   | 62  |
| Season and Interannual Variability in Particulate Matter Size and Composition .....                    | 63  |
| 4. <i>Single Particle Characterization in Riverside, CA during the SOAR 2005 Campaign: Seasonal</i>    |     |
| Comparisons .....  | 63  |
| i. Introduction.....   | 63  |
| ii. Experimental .....   | 64  |
| a. SOAR Campaign .....   | 64  |
| c. ATOFMS Data Analysis.....   | 65  |
| iii. Results and Discussion .....  | 66  |
| a. PM <sub>2.5</sub> Concentrations .....  | 67  |
| b. Chemical Composition of ART-2a Clusters.....  | 68  |
| c. SOAR-I Diurnal Variation.....   | 72  |
| d. SOAR-II Episodic Variations.....  | 76  |
| e. SOAR-I and SOAR-II Comparison .....   | 80  |
| iv. Acknowledgements .....   | 83  |
| 5. <i>Seasonal Volatility Dependence of Ambient Particle Phase Amines .....</i>                        | 85  |
| i. Introduction.....   | 85  |
| ii. Experimental .....   | 86  |
| a. Ambient Measurements .....  | 86  |
| b. Amine Mass Calibration.....   | 88  |
| iii. Results and Discussion .....  | 94  |
| iv. Acknowledgements .....   | 103 |
| 6. <i>Inter-annual Comparison of Ambient, Single-Particle Chemical Mixing State in Riverside, CA..</i> | 104 |
| i. Introduction.....   | 104 |
| ii. Experimental .....   | 105 |
| iii. Results and Discussion .....  | 106 |
| a. Impact of meteorology on particulate mass concentrations .....                                      | 106 |
| b. Overall submicron aerosol chemical composition.....   | 110 |
| c. Assessment of single-particle mixing state and particle aging .....                                 | 110 |
| d. Relating particle chemistry to meteorology and PM <sub>2.5</sub> mass concentrations .....          | 113 |
| iv. Conclusions.....   | 117 |
| v. Acknowledgements .....  | 118 |

|  |     |
|--|-----|
| Mass Comparisons and Investigations into the Volatile and Semivolatile Fraction of Particles .....   | 120 |
| 7. <i>Comparison of Two Methods for Obtaining Quantitative Mass Concentrations from Aerosol Time-of-Flight Mass Spectrometry Measurements</i> .....  | 120 |
| i. Introduction.....   | 120 |
| ii. Experimental .....   | 121 |
| a. ATOFMS Data Acquisition .....   | 121 |
| b. MOUDI Measurements .....  | 122 |
| c. APS Measurements.....   | 122 |
| iii. Results and Discussion .....  | 122 |
| a. Scaling with MOUDI.....   | 122 |
| b. Scaling with the APS.....   | 128 |
| c. PM <sub>2.5</sub> Measurement Intercomparison .....   | 134 |
| iv. Conclusions.....   | 136 |
| v. Acknowledgements .....  | 137 |
| 8. <i>The Effect of APS Scaling Functions on the Quantification of Aerosol Time-of-Flight Mass Spectrometry Measurements</i> .....   | 138 |
| i. Introduction.....   | 138 |
| ii. Experimental .....   | 139 |
| a. CRPAQS ATOFMS Measurements and Data Analysis .....  | 139 |
| b. Reference Studies with APS Scaling Functions .....  | 140 |
| c. The Calculation of the Scaling Functions in Reference Studies .....   | 141 |
| iii. Results and Discussion .....  | 141 |
| a. Scaling Curves and Scaling Functions.....   | 141 |
| b. Major Particle Types in CRPAQS.....   | 142 |
| c. Scaled ATOFMS Mass Concentrations .....   | 144 |
| d. APS Scaled Particle Mass Fraction .....   | 146 |
| iv. Conclusions.....   | 148 |
| v. Acknowledgements .....  | 149 |
| Changes in Size-Resolved Particle Composition Linked with Meteorology Measurements and Air Mass Back Trajectories to Increase Understanding of Sources and Secondary Contributions to Particulate Matter ..... | 150 |
| 9. <i>Characterization of trace metals in single urban particles during the SOAR 2005 campaign</i> .....   | 150 |
| i. Introduction.....   | 150 |
| ii. Experimental .....   | 151 |
| a. Sampling Location.....  | 151 |
| b. Instrumentation.....  | 151 |
| c. Data analysis.....  | 151 |
| iii. Results and Discussion .....  | 152 |
| iv. Acknowledgements.....  | 165 |
| 10. <i>Impact of Emissions from the Los Angeles Port Region on San Diego Air Quality During Regional Transport Events</i> .....  | 166 |
| i. Introduction.....   | 166 |
| ii. Experimental .....   | 166 |
| a. Scripps Institution of Oceanography of Pier 2006 Study.....   | 166 |
| b. Real-Time Single Particle Mass Spectrometry .....   | 167 |
| c. Data Analysis.....  | 167 |
| d. Scaling ATOFMS to Mass Concentrations .....   | 167 |
| iii. Results and Discussion .....  | 168 |
| a. Mass Concentrations Across San Diego County .....   | 170 |
| b. Identification of Regional Events .....   | 171 |
| c. Air Mass History during Regional Events .....   | 171 |
| d. Particle Chemistry during Regional Transport Events .....   | 173 |
| e. General submicron particle types .....  | 175 |
| f. Sulfate Formation and Aging Processes During Transport.....   | 176 |
| g. Temporal Variations by Particle Type.....   | 177 |
| h. Correlation between Major Particle Types .....  | 178 |

|  |     |
|--|-----|
| i. Size-Resolved Chemistry of Regional Events.....   | 179 |
| i. Correlation between Ships at Sea and Selected Particle Types .....  | 179 |
| j. Impact of Regional Events .....   | 180 |
| iv. Acknowledgements .....   | 181 |
| 11. <i>Single Particle Composition, Hygroscopicity, and CCN Activity during the 2007 San Diego Wildfires</i> .....   | 182 |
| i. Introduction.....   | 182 |
| ii. Experimental .....   | 183 |
| a. Sampling locations and instrumentation .....  | 183 |
| b. ATOFMS data analysis .....  | 184 |
| c. Single hygroscopicity parameter .....   | 184 |
| iii. Results and Discussion .....  | 185 |
| a. Temporal trends of UCSD CCN_0.3, UCSD CN .....  | 187 |
| b. Composition, size and CCN .....   | 187 |
| c. Air Mass and hygroscopicity .....   | 190 |
| iv. Conclusions.....   | 191 |
| v. Acknowledgements .....  | 192 |
| Development of Source Apportionment Algorithms .....   | 193 |
| 12. <i>Using mass spectral source signatures to apportion exhaust particles from gasoline and diesel powered vehicles in a freeway study using UF-ATOFMS</i> ..... | 193 |
| i. Introduction.....   | 193 |
| ii. Experimental .....   | 194 |
| iii. Results and Discussion .....  | 195 |
| a. Creation and Comparison of Particle Seeds From Source Studies .....   | 195 |
| b. Particles Detected that Match to HDDV/LDV Source Seeds.....   | 199 |
| c. Temporal Trends and Correlations with UF-ATOFMS Data .....  | 202 |
| iv. Acknowledgements.....  | 210 |
| 13. <i>Source apportionment of freeway-side PM<sub>2.5</sub> using ATOFMS</i> .....  | 211 |
| i. Introduction.....   | 211 |
| ii. Experimental .....   | 211 |
| iii. Results and Discussion .....  | 213 |
| a. Quality Assurance of ATOFMS Data.....   | 213 |
| b. Comparison with standard particle counts.....   | 214 |
| c. Comparison of particle phase and gas phase data.....  | 216 |
| d. Comparison of temporal trends from peripheral instruments.....  | 217 |
| e. Upwind/Downwind Sampling .....  | 219 |
| f. Data Analysis Used for Apportionment .....  | 228 |
| g. Source Apportionment Using ART-2a .....   | 229 |
| h. Size Resolved Source Apportionment Temporal Series.....   | 231 |
| iv. Acknowledgements.....  | 234 |
| 14. <i>Aging effects on source apportionment from the single particle perspective</i> .....  | 235 |
| i. Introduction.....   | 235 |
| ii. Experimental .....   | 236 |
| a. Sampling location and instrumentation .....   | 236 |
| b. Data analysis.....  | 236 |
| iii. Results and Discussion .....  | 237 |
| a. Source signature library matching .....   | 237 |
| b. Aging effects .....   | 245 |
| c. Secondary species as aging markers .....  | 254 |
| iv. Acknowledgements.....  | 258 |
| III. Summary and Conclusions .....   | 259 |
| IV. References .....   | 261 |
| V. Appendices .....  | 295 |
| Publications and Presentations.....  | 295 |
| 1. Publications .....  | 295 |
| 2. Presentations .....   | 296 |





## LIST OF FIGURES

|  |    |
|--|----|
| Figure 1: Instrument schematic diagrams of the (a) ATOFMS and (b) UF-ATOFMS. ....  | 3  |
| Figure 2: Hourly UF-ATOFMS counts of single particles for which chemical information was obtained as a function of aerodynamic diameter during the summer (top) and fall (bottom). ....  | 18 |
| Figure 3 Representative mass spectra for the general chemical classes of ultrafine particles as determined by the UF-ATOFMS. “CT” in the negative spectra represents crosstalk due to the interference of extremely intense peaks in the positive polarity. ....   | 19 |
| Figure 4 Relative size distribution (10 nm bins) of ultrafine particle types during the summer (a) and fall (b). The black trace represents the total number of ultrafine particles chemically analyzed by the UF-ATOFMS in each 10 nm size bin. ....  | 20 |
| Figure 5 Hourly relative fractions of ultrafine particle types during the summer (top) and fall (bottom). The black trace represents the hourly total of ultrafine particles (50-100 nm) chemically analyzed by the UF-ATOFMS. ....  | 21 |
| Figure 6: Temporal trends of gas- and particle-phase measurements, as well as meteorological variables, for one week (Sunday through Saturday) during the summer season. ....  | 22 |
| Figure 7: Temporal trends of gas- and particle-phase measurements, as well as meteorological variables, for one week (Sunday through Saturday) during the fall season. ....  | 26 |
| Figure 8: Map showing the Port of LA. The green diamond represents the sampling location and the red markers and line represent the one minute resolution positions and course of a container ship as it departed from the Port of LA at 03:30 on November 19, 2007. The blue line represents the average wind direction during transport of the plume to the sampling location. ....  | 32 |
| Figure 9: Identification of the plume of Container 1b. Gas phase measurements included SO <sub>2</sub> (orange), NO <sub>x</sub> (green), and O <sub>3</sub> (blue). Particle phase measurements were of black carbon (black), particle number concentration (white), and size-resolved number concentrations over time (color matrix). ....   | 33 |
| Figure 10: Average negative and positive ion mass spectra for the OC-V-sulfate (a) and fresh soot (b) particle types. ....   | 35 |
| Figure 11: A digital color stack for the OC-V-sulfate particle type showing the fraction of particles containing a specific peak on the y-axis versus mass-to-charge on the x-axis. The color represents the fraction containing a specific range of peak areas, with 500 being the lower peak area cutoff. The top portion of the figure represents the positive mass spectrum and the bottom portion represents the negative mass spectrum. .... | 37 |
| Figure 12: A digital color stack for the fresh soot particle type showing the fraction of particles containing a specific peak on the y-axis versus mass-to-charge on the x-axis. The color represents the fraction containing a specific range of peak areas, with 500 being the lower peak area cutoff. The top portion of the figure represents the positive mass spectrum and the bottom portion represents the negative mass spectrum. ....   | 38 |

|  |    |
|--|----|
| Figure 13: Average mass spectrum of the Ca-ECOC particle type from a fresh soot plume.....   | 39 |
| Figure 14: Average mass spectra of background particle types before and after the plume from Container1a. ....   | 40 |
| Figure 15: Average mass spectra of background particle types from before and after the plume from Container4. CT represents crosstalk on the detector.....   | 41 |
| Figure 16: Time series of the differential counting rate (number of ATOFMS counts per 2 minutes) for the OC-V-sulfate and fresh soot particle types. Peaks that could be correlated with ships are labeled; plumes with asterisks were only tentatively identified. ....   | 42 |
| Figure 17: Size-resolved number fractions of the different particle types for the background before and after a) OC-V-sulfate (Container4) and b) fresh soot (Container1a) plumes. (c,d) Size-resolved chemical fractions of these plumes. ....  | 43 |
| Figure 18: Average sulfate (red circles) and sulfuric acid (blue circles) absolute peak areas for major particle types during the plume of the vessel Container4; errors are shown by 95% confidence intervals. Number fractions of particles containing sulfate (red diamond) and sulfuric acid (blue diamond) are shown. The inset shows a zoomed-in version of particle types with lower peak areas than the OC-V-sulfate type.....   | 44 |
| Figure 19: Map of the San Diego metropolitan area around San Diego Bay with trailer sampling sites and air pollution control district (APCD) sites, as well as 200 meter HYSPLIT air mass back trajectories for (a) February 12, 2009 and (b) March 13, 2009.....  | 49 |
| Figure 20: Comparison of meteorology conditions (temperature-red, relative humidity-light blue, wind speed-grey, wind direction-black markers) and gas phase concentrations ( $O_3$ -blue, $NO_x$ -green, $SO_2$ -gold) on February 12 <sup>th</sup> and March 13 <sup>th</sup> ..   | 52 |
| Figure 21: (a) $PM_{2.5}$ mass concentration data at each site for the: Scaled ATOFMS mass (blue bars), trailer BAM (red bars), and DT-APCD BAM (green bars). (b) Number concentration by site from summed SMPS scans (gold bars).....   | 54 |
| Figure 22: Size distribution measurements (SMPS and APS) for February 12 <sup>th</sup> and March 13 <sup>th</sup> as measured at the trailer sampling sites. The red traces correspond to Silver Strand, green traces to Cesar Chavez Park, yellow to Coronado, blue to Chula Vista, and purple to Pepper Park .....   | 56 |
| Figure 23: Chemically-resolved relative mass fractions of particle types for (a) submicron (0.523 – 1 $\mu m$ ) and (b) supermicron (1-2.5 $\mu m$ ) particles at each site. The black diamonds represent the ATOFMS mass concentration by site. ....  | 59 |
| Figure 24: Peak areas related to aging for (a) Sea salt particles, (b) Biomass particles, and (c) ECOC particles. For sea salt particles, chloride (blue – $^{35}Cl^-$ ) and nitrate (green – $^{62}NO_3^-$ ) are plotted. For biomass and ECOC particles, nitrate and sulfate (purple – $m/z$ $^{97}HSO_4^-$ ) are plotted. The ratio of the peak areas for nitrate and sulfate (d) are given for biomass and ECOC particle types. .... | 61 |
| Figure 25: Map of SOAR sampling site on UCR campus. ....   | 65 |
| Figure 26: Temporal variations of ambient wind speed, wind direction, temperature, relative humidity, and ozone concentration during SOAR-I (a) and SOAR-II (b)...   | 67 |
| Figure 27: Hourly temporal variations of BAM $PM_{2.5}$ mass concentration and size-resolved hourly APS $PM_{2.5}$ particle number concentration during SOAR-I (top) and   |    |

|  |    |
|--|----|
| SOAR-II (bottom). Contour plots represent APS number concentration in log scale, and the red lines correspond to BAM data.....   | 68 |
| Figure 28: Hourly temporal variations of O <sub>3</sub> concentration and hourly average peak area of m/z 43. ....   | 69 |
| Figure 29: ART-2a weight matrices of representative particle types during SOAR-I and SOAR-II. ....   | 71 |
| Figure 30: Temporal variations of the number fractions of major particle types for the top 50 clusters superimposed with PM <sub>2.5</sub> mass concentrations (red line) and size distributions of total ATOFMS particle counts. ....   | 73 |
| Figure 31: Hourly size-resolved number fractions of SOAR-I top 50 clusters from ART-2a results averaged for 3:00, 9:00, 15:00 and 21:00 over all sampling days. Size resolution is 0.05 μm for the submicron range and 0.10 μm for the supermicron range.....  | 74 |
| Figure 32: Size-resolved number fractions of SOAR-II top 50 clusters from ART-2a results averaged over each episode along with corresponding PM <sub>2.5</sub> levels and representative 48-hour HYSPLIT back trajectories.....  | 78 |
| Figure 33: Ternary plots of SOAR-I and SOAR-II submicron aged OC1 particles. In each plot, a particle mostly containing nitrate would appear at the lower left vertex, a particle mostly containing sulfate would appear at the lower right vertex, a particle mostly containing ammonium would appear at the top vertex. ....                                 | 81 |
| Figure 34: Temporal variation of the mass concentration of major ATOFMS particle types. Mass concentrations are obtained by scaling ATOFMS measurements with APS measurements. ....  | 83 |
| Figure 35: Size-resolved chemical composition of unheated particles during (a) SOAR-1 (summer) and (b) SOAR-2 (fall). Size resolution is 10 nm and 50 nm for the ranges of 100-350 nm and 350-1000 nm, respectively. The majority of the particles greater than ~150 nm show evidence of internally mixed organic carbon, ammonium, nitrate, and sulfate. .... | 88 |
| Figure 36: Amine mass calibration experimental set-up (MFC = mass flow controller; TEA = triethylamine; DMA = differential mobility analyzer; CPC = condensation particle counter; ATOFMS = aerosol time-of-flight mass spectrometer).....   | 89 |
| Figure 37: Size distributions of uncoated (solid) and TEA-coated (dashed) 270 nm PSLs. SMPS distributions of mobility diameter are shown in red; ATOFMS distributions of vacuum aerodynamic diameter are in black. The arrows indicate the shifts of the respective distributions. ....  | 91 |
| Figure 38: Average mass spectra of (a) PSLs coated with TEA and (b) uncoated 270 nm PSLs. The inset shows a comparison of the m/z 86 peak intensities. ....  | 92 |
| Figure 39: Absolute area of m/z 86 vs vacuum aerodynamic diameter for the TEA-coated PSLs. ....  | 92 |
| Figure 40: Absolute area of m/z 86 vs derived TEA mass for the TEA-coated PSLs. ....   | 94 |
| Figure 41: Average positive and negative mass spectra of the unheated aged OC (nitrate-sulfate) particles during (a) summer and (b) fall. Peak areas are reported in arbitrary units (A.U.). ....  | 95 |
| Figure 42: Positive and negative mass spectra of a single particle exhibiting m/z 130 measured during TEA-nitric acid chamber experiments. ....  | 96 |

- Figure 43: Summer (a,b) and fall (c,d) ternary plots show the relative distributions of peak areas of ammonium ( $m/z$  18 ( $\text{NH}_4^+$ )), amines ( $m/z$  86 ( $(\text{C}_2\text{H}_5)_2\text{NCH}_2^+$ )), nitrate ( $m/z$  -62 ( $\text{NO}_3^-$ )), and sulfate ( $m/z$  -97 ( $\text{HSO}_4^-$ )) for the unheated and heated (54-230°C) aged OC (nitrate-sulfate) particles. Random samples of ~2,000 single particles are plotted for each temperature. .... 97
- Figure 44: For aged OC (nitrate-sulfate) particles, the (a) fraction of  $m/z$  86 peak area remaining over the range of thermodenuder temperatures from 54-230 °C is shown relative to the unheated particles (ambient temperature averages of 22.9 °C and 15.6 °C in the summer and fall, respectively). In addition, the (b) amine mass/particle and (c) amine mass percent/particle are shown for each temperature. .... 98
- Figure 45: Relative fractions of nitrate ( $m/z$  -62 ( $\text{NO}_3^-$ )) remaining on the aged OC (nitrate-sulfate) particles at each TD temperature during SOAR-1 and SOAR-2. ... 99
- Figure 46: Relative acidity ratios for summer and fall for each thermodenuder period (unheated, 54°C, 83°C, 113°C, 142°C, 171°C, 201°C, 230°C) for the aged OC (nitrate-sulfate) particles. The ratios are defined as the sum of the absolute average peak areas of nitrate ( $m/z$  -62 ( $\text{NO}_3^-$ )) and sulfate ( $m/z$  -97 ( $\text{HSO}_4^-$ )) divided by ammonium ( $m/z$  18 ( $\text{NH}_4^+$ )) or the sum of ammonium and amines ( $m/z$  86 ( $(\text{C}_2\text{H}_5)_2\text{NCH}_2^+$ )). .... 102
- Figure 47: Illustrates the temporal profiles of gas-phase  $\text{O}_3$  (ppb, green line), relative humidity (% , blue line), temperature (°C, orange line),  $\text{PM}_{2.5}$  mass concentrations ( $\mu\text{g}/\text{m}^3$ , black line), and wind speed (m/s, grey line) from the three summer studies in Riverside, CA. Plot a) has data from July 29 – August 15, 2005, b) August 10 – 21, 2006, and c) August 29 – September 7, 2007. Trends of these measurements are discussed in the main manuscript. .... 108
- Figure 48: Representative 48-hour HYSPLIT air mass back trajectories in Riverside for a) 2005, b) 2006, and c) 2007. Trajectories are labeled by source wind direction and terrain. The sampling site is represented by the star in each map..... 109
- Figure 49: Mixing states of secondary species in major particle types from a) 2005, b) 2006, and c) 2007. The abscissa contains major ATOFMS particle types and the y-axis contains secondary species markers  $\text{C}_2\text{H}_3\text{O}^+$  ( $m/z$  43),  $(\text{C}_2\text{H}_5)_2\text{NCH}_2^+$  ( $m/z$  86),  $\text{NH}_4^+$  ( $m/z$  18),  $\text{HSO}_4^-$  ( $m/z$  -97),  $\text{NO}_2^-$  ( $m/z$  -46), and  $\text{NO}_3^-$  ( $m/z$  -62). The color scale represents the number fraction of particles within a single particle type that contained each specific marker (secondary species). .... 111
- Figure 50: shows the ratio of the sum of peak areas  $m/z$  43 to  $m/z$  37 plotted as a function of  $\text{O}_3$  concentration (ppm) from a) 2005, b) 2006, and c) 2007 with maroon being the lowest concentration and blue being the highest. Also pictured is the temporal profile of  $\text{PM}_{2.5}$  mass concentrations ( $\mu\text{g}/\text{m}^3$ ). .... 113
- Figure 51: Temporally-resolved submicron particle chemistry from a) 2005, b) 2006, and c) 2007. Hourly  $\text{PM}_{2.5}$  mass concentrations are also plotted for each year (black line). .... 115
- Figure 52: Temporally-resolved relative number fraction of ECOC particle types (red diamonds) from a) 2005, b) 2006, and c) 2007. The black shaded regions are the  $\text{PM}_{2.5}$  mass concentrations for each year. .... 116
- Figure 53: Size resolved submicron particle chemistry in Riverside, CA. .... 117
- Figure 54: (a) Linear interpolation over the Fresno high-miss period to obtain estimated hit counts and estimated missed counts for the period of January 28th, 3:35 – 11:15;

|  |     |
|--|-----|
| (b) estimated missed particle recording time vs. missed particle detection rate for all five high-miss periods with a time resolution of 6 minutes for Fresno dataset. ....  | 124 |
| Figure 55: Comparison of scaled ATOFMS mass concentrations and MOUDI measurements in Fresno.....   | 127 |
| Figure 56: Temporal variation of hourly BAM and scaled ATOFMS PM <sub>2.5</sub> mass concentrations in Fresno. The scaling function for the ATOFMS was obtained by comparison with MOUDI measurements. ....  | 128 |
| Figure 57: APS scaling curve for Angiola measurements. (a) hourly scaling curve for February 03, except for 13:00; (b) exponential regression of left half of scaling curve at 22:00; (c) polynomial regression of right half of scaling curve at 22:00.....   | 130 |
| Figure 58: Correlations between BAM and APS scaled ATOFMS mass concentrations. (a) ATOFMS mass concentrations are obtained with single density ( $\rho$ ) values for all particles ( $\rho = 1.8 \text{ g}\cdot\text{cm}^{-3}$ , $\rho = 1.9 \text{ g}\cdot\text{cm}^{-3}$ , or $\rho = 2.0 \text{ g}\cdot\text{cm}^{-3}$ ); (b) ATOFMS mass concentrations are obtained with different density pairs for submicron and supermicron particles: 1.2 and $2.7 \text{ g}\cdot\text{cm}^{-3}$ , 1.7 and $2.2 \text{ g}\cdot\text{cm}^{-3}$ , 1.7 and $2.7 \text{ g}\cdot\text{cm}^{-3}$ , 1.7 and $3.2 \text{ g}\cdot\text{cm}^{-3}$ , and 2.2 and $2.7 \text{ g}\cdot\text{cm}^{-3}$ . .... | 132 |
| Figure 59: Temporal variation of Angiola particulate mass concentrations obtained with BAM and APS scaled ATOFMS ( $\rho = 1.9 \text{ g}\cdot\text{cm}^{-3}$ ). ....   | 133 |
| Figure 60: APS scaling curves for all studies, including TexAQS, NC-CCS-I, NC-CCS-II, CIFEX, Freeway, APMEX, and Angiola studies.....  | 142 |
| Figure 61: Size-resolved un-scaled particle type mass concentrations and mass fractions for Fresno and Angiola. (a) un-scaled particle type mass concentrations in Fresno (b) un-scaled particle type mass fractions in Fresno (c) un-scaled particle type mass concentrations in Angiola (d) un-scaled particle type mass fractions in Angiola. ....  | 143 |
| Figure 62: Fresno and Angiola size-resolved particle type mass concentrations scaled with TexAQS and APMEX scaling functions. (a) Fresno particle type mass concentrations with TexAQS APS scaling function (b) Fresno particle type mass concentrations with APMEX APS scaling function (c) Angiola particle type mass concentrations with TexAQS APS scaling function (d) Angiola particle type mass concentrations with APMEX APS scaling function. ....  | 145 |
| Figure 63: Fresno and Angiola individual particle type mass fractions for submicron, supermicron and PM <sub>2.5</sub> range obtained with APS scaling functions from TexAQS, Freeway, CIFEX, NC-CCS, APMEX, and Angiola studies. ....   | 147 |
| Figure 64: Trends of the three main vanadium particle types: representative mass spectra (a-c); half-hourly temporal variations in summer (d) and fall (e); size-resolved total particle fractions in summer (f) and fall (g); and half-hourly wind direction profiles based on particle counts (h-j). ....  | 154 |
| Figure 65: Half-hourly wind direction and wind speed (color scale) distribution for all PM <sub>2.5</sub> particle types in summer (a) and fall (b). ....  | 155 |
| Figure 66: Half-hourly wind direction based on time of day for summer (a) and fall (b). Note that for the summer season, the meteorological data ended at 12:00 on August 14 <sup>th</sup> . ....  | 156 |
| Figure 67: Reported annual atmospheric emissions of the specified metal and metal compounds in Riverside, Los Angeles, Orange, and San Bernardino counties in 2005 based on the data from the Environmental Protection Agency (EPA) Toxics Release Inventory (TRI). ....   | 157 |

|  |     |
|--|-----|
| Figure 68: Trends of the three main iron particle types: representative mass spectra (a-c); half-hourly temporal variations in summer (d) and fall (e); size-resolved total particle fractions in summer (f) and fall (g); and half-hourly wind direction profiles based on particle counts (h-j).   | 158 |
| Figure 69: Trends of the three main zinc particle types: representative mass spectra (a-c); half-hourly temporal variations in summer (d) and fall (e); size-resolved total particle fractions in summer (f) and fall (g); and half-hourly wind direction profiles based on particle counts (h-j).   | 160 |
| Figure 70: Trends of the three main barium particle types: representative mass spectra (a-c); half-hourly temporal variations in summer (d) and fall (e); size-resolved total particle fractions in summer (f) and fall (g); and half-hourly wind direction profiles based on particle counts (h-j).   | 161 |
| Figure 71: Trends of the three main lead particle types: representative mass spectra (a-c); half-hourly temporal variations in summer (d) and fall (e); size-resolved total particle fractions in summer (f) and fall (g); and half-hourly wind direction profiles based on particle counts (h-j).   | 162 |
| Figure 72: A) The lower portion of the graph shows time series of scaled PM <sub>2.5</sub> mass concentrations at the SIO Pier (red line) and PM <sub>2.5</sub> data from downtown San Diego (black line). B) Hourly size distributions measured by an aerodynamic particle sizer (APS) from 0.5-1 $\mu\text{m}$ from August 17, 2006 – October 2, 2006. The overlaid blue line is the sum of ATOFMS counts in the 0.5-1 $\mu\text{m}$ size range per hour. C) Scaled PM <sub>1</sub> (green line) and PM <sub>2.5</sub> (red line) mass concentrations are shown over the sampling period. The gray dashed line represents the average PM <sub>1</sub> mass concentration during the study, and the black dashed line represents the PM <sub>1</sub> threshold set for regional events. | 169 |
| Figure 73: Fraction of scaled PM <sub>2.5</sub> corresponding to PM <sub>1</sub> hourly.   | 170 |
| Figure 74: HYSPLIT (24 hour) back trajectory analysis at 500 meters for the peak hour of each regional event. Large diamonds represent 24 hours back from the source and small diamonds present 12 hours. A) Trajectories in red pass near the LA Port while trajectories in blue pass over the SD Port. B) Trajectories in purple are representative of non-transport time periods. C) The table included displays the frequency of different air mass types and source regions, as well as the number of regional events observed during each back trajectory type.  | 173 |
| Figure 75: Average negative and positive ion mass spectra for a) ECOC(sulfate-nitrate) and b) V-Ni-Fe(sulfate-nitrate) particles. c) Time series of hourly ECOC(sulfate-nitrate) and V-Ni-Fe(sulfate-nitrate) particle type counts.  | 174 |
| Figure 76: Average negative and positive ion mass spectra for the top six particle types (excluding ECOC and V-Ni-Fe which are discussed in the main paper): a) Elemental carbon, b) Organic carbon, c) Biomass Burning, d) Sea salt, e) Sea salt with soot.   | 176 |
| Figure 77: a) Time series of the relative fractions of submicrometer particles types b) Time series of counts of submicron particle types. The black line on both plots is the scaled PM <sub>1</sub> mass concentration ( $\mu\text{g}/\text{m}^3$ ).   | 178 |
| Figure 78: Comparison of the average size-resolved mass distributions of major particle types during regional events and non-events.   | 179 |
| Figure 79: Time series of hourly counts of the ECOC and V-Fe-Ni particle types during 6 day period with ship positions recorded per hour.  | 180 |

|  |     |
|--|-----|
| Figure 80: HYSPLIT back trajectories during wildfire sampling period. Each line is a representative 48 hour backtrajectory during that period at 500m. Corresponding periods for comparison to sampling data are in parenthesis. ....  | 187 |
| Figure 81: Overview of Urey Hall CCN (UCSD CCN_0.3) and SIO CCN (SIO CCN_0.1) concentrations (s=0.29, 0.13 respectively), fCCN_0.3, fCCN_0.1, Dact_0.3, meteorological data and Urey Hall SMPS .....   | 187 |
| Figure 82: Particle classification temporal. Shown is the classification of particles detected between 50 and 300 nm by the ATOFMS during the study. Biomass is shown in red and is the dominant type during most of the period. Gray is elemental carbon (EC) and grows in as biomass decreases. ....   | 188 |
| Figure 83: Comparison of CCN_0.3 and CCN_0.1 for entire study. ....  | 189 |
| Figure 84: Single parameter hygroscopicity (Kappa) values of the particles during different air mass periods for CCN_0.3. The top of the boxes are the 3 <sup>rd</sup> quartile of kappa values for that period, the bottoms are the 1 <sup>st</sup> quartile values for that period. Whiskers show the minimum and maximum values for each period. Median values are the middle lines dividing the top and bottom of the boxes. Black diamonds are average CCN concentrations for those periods with standard deviation as error bars. .... | 189 |
| Figure 85: Single parameter hygroscopicity (Kappa) values of the particles during different air mass periods for CCN_0.1. The top of the boxes are the 3 <sup>rd</sup> quartile of kappa values for that period, the bottoms are the 1 <sup>st</sup> quartile values for that period. Whiskers show the minimum and maximum values for each period. Median values are the middle lines dividing the top and bottom of the boxes. Black diamonds are average CCN concentrations for those periods with standard deviation as error bars. .... | 190 |
| Figure 86: Dot product comparisons of the representative area matrices between the general classes from the HDDV and LDV dynamometer experiments using UF-ATOFMS. Classes are labeled in the same manner as in the manuscripts from Sodeman <i>et al.</i> 2005 and Toner <i>et al.</i> 2006. ....  | 197 |
| Figure 87: ART-2a matching error analysis using non-exclusive matching of HDDV and LDV dynamometer particles. For each, the fraction of HDDV and LDV particles that matched to the HDDV, LDV, or both HDDV and LDV clusters from the HDDV/LDV reference library are shown for ultrafine (50–100nm) and accumulation (100–300nm) mode particles.....  | 198 |
| Figure 88: ART-2a matching error analysis using exclusive matching of HDDV and LDV dynamometer particles. For each, the fraction of HDDV and LDV particles that matched to the HDDV or LDV clusters from the HDDV/LDV reference library are shown for ultrafine (50–100nm) and accumulation (100–300nm) mode particles. ....   | 199 |
| Figure 89: Weight matrices of the top particle types detected during freeway study that match to vehicle study signatures. ....  | 201 |
| Figure 90: Temporal plots of A) NO <sub>x</sub> gas data vs. aethalometer data; and B) HDDV video counts vs. aethalometer data. Both NO <sub>x</sub> and aethalometer data show a good correlation with each other ( $R^2 = 0.7$ ). The HDDV video counts also track the aethalometer data. ....   | 203 |
| Figure 91: Top: Wind data (blowing from: N = 0°/360°, E = 90°, S = 180°, W = 270°) along with LDV & HDDV traffic counts (from video). HDDV counts are multiplied   |     |

|  |     |
|--|-----|
| by 20 to keep them on the same scale as LDV traffic counts. Middle: HDDV/LDV/Other ART-2a matching result unscaled counts from UF-ATOFMS data. Bottom: HDDV/LDV/Other ART-2a matching fraction results from UF-ATOFMS data. Data shown are accumulation mode particles ( $D_a = 100\text{--}300\text{nm}$ ) for July 24 to Aug 03, 2004.....   | 205 |
| Figure 92: Top: SMPS data along with LDV & HDDV traffic counts (from video). HDDV counts are multiplied by 20 to keep them on the same scale as LDV traffic counts. Middle: HDDV/LDV/Other ART-2a matching result unscaled counts from UF-ATOFMS data. Bottom: HDDV/LDV/Other ART-2a matching fraction results from UF-ATOFMS data. Data shown are ultrafine mode particles ( $D_a = 50\text{--}100\text{nm}$ ) for July 24 to Aug 03, 2004. ....                              | 207 |
| Figure 93: Time series of aethalometer data with HDDV/LDV apportioned particles. The $R^2$ values for aethalometer to HDDV is 0.77, and 0.56 for the aethalometer to LDV. ....   | 209 |
| Figure 94: A) QA plot of UF-ATOFMS particle scatters vs. particles scattered that produced a mass spectrum to determine if there are any chemical biases or particle types being missed. B) Comparison of the two standard inlet ATOFMS instruments particle detections when running side-by-side at the freeway site. Plots are in one hour resolution. ....  | 214 |
| Figure 95: A) Comparison of sub-100 nm particle counts with the SMPS to sub-100 nm particles detected (that produced mass spectra) with the UF-ATOFMS at the freeway site. B) Comparison of fine mode particles (500 – 1000 nm) with the APS to fine mode particles (200 – 1000 nm) detected (that produced mass spectra) with the standard inlet ATOFMS at the freeway site. Plots are in one hour resolution. ....   | 215 |
| Figure 96: A) Comparison of sub-100 nm UF-ATOFMS particles detected that produced mass spectra with CO measurements. B) Comparison of sub-100 nm UF-ATOFMS particles detected that produced mass spectra with $\text{NO}_x$ measurements. C) Comparison of CO and $\text{NO}_x$ measurements at the freeway site. Plots are in one hour resolution.....  | 217 |
| Figure 97: A) Comparison of aethalometer and $\text{NO}_x$ measurements at the freeway site. B) Comparison of aethalometer and nephelometer measurements at the freeway site. Plots are in one hour resolution. ....   | 219 |
| Figure 98: A) SMPS and APS particle number concentrations at the freeway site from. B) SMPS and APS particle number concentrations at the upwind sampling site. Both plots are shown from Jul. 24 to Aug. 3, 2004 in order to directly compare the two sites. The data is shown in log scale. ....   | 221 |
| Figure 99: Particle size distribution data of: A) Standard inlet ATOFMS at the upwind sampling site. B) Standard inlet ATOFMS at the freeway sampling site. C) UF-ATOFMS at the freeway site. The particle size data shown is only for particles that were detected that produced a mass spectrum with the particular ATOFMS instrument. The data shown is from Jul. 24 to Aug. 3, 2004 in order to compare the two sites and to the APS and SMPS data shown in Figure 98..... | 223 |
| Figure 100: Positive and negative ion mass spectra for the regional background (A) vanadium and (B) EC particle types. (C) The temporal trends of the vanadium particle type detected with all three ATOFMS instruments compared to wind data.   |     |



|  |     |
|--|-----|
| (D) Temporal trends (and correlation) of total background vanadium particles versus the total background EC particles for the three ATOFMS instruments.....  | 225 |
| Figure 101: Hourly HYSPLIT model 24-hour back trajectories at 500 m for each day at the freeway study site.....  | 227 |
| Figure 102: Size resolved source apportionment of the particles detected at the upwind (top) and freeway (bottom) sampling sites. Both plots are averages for ATOFMS data acquired from July 24 to Aug 3, 2004. In the bottom plot for the freeway site, the sizing region of overlap between the UF-ATOFMS and standard inlet ATOFMS is 200 – 300 nm..... | 230 |
| Figure 103: Time series of the size segregated source apportionment fractions for the freeway site ultrafine and accumulation mode particles detected with the UF-ATOFMS and ATOFMS. ....  | 233 |
| Figure 104: Hourly temporal series of the size segregated source apportionment fractions (VF = 0.85) for the summer SOAR ultrafine (UF), small accumulative mode (SAM), large accumulation mode (LAM), submicron (SUB), and supermicron (SUPER) particles detected with the UF-ATOFMS and ATOFMS. ....   | 240 |
| Figure 105: Hourly temporal series of the size segregated source apportionment fractions (VF = 0.85) for the fall SOAR ultrafine (UF), small accumulative mode (SAM), large accumulation mode (LAM), submicron (SUB), and supermicron (SUPER) particles detected with the UF-ATOFMS and ATOFMS. ....   | 241 |
| Figure 106: Number of summer particles matched to each source seed for a) UF (50-100 nm), b) SAM (100-140 nm), c) LAM (140-400 nm), d) SUB (140-1000 nm), and e) SUPER (1000-3000 nm) particles. ....  | 242 |
| Figure 107: Number of fall particles matched to each source seed for a) UF (50-100 nm), b) SAM (100-140 nm), c) LAM (140-400 nm), d) SUB (140-1000 nm), and e) SUPER (1000-3000 nm) particles. ....  | 243 |
| Figure 108: Average source contribution particles matched to the source library at different VF per size bin. ....   | 247 |
| Figure 109: Average mass spectra obtained by lowering the matching factor for summer SOAR LAM (140-400 nm) particles apportioned to LDV.....   | 248 |
| Figure 110: Hourly temporal series of the size segregated source apportionment fractions (VF = 0.85) for the summer SOAR ultrafine (UF), small accumulative mode (SAM), large accumulation mode (LAM), submicron (SUB), and supermicron (SUPER) particles using the updated source signature library. ....   | 249 |
| Figure 111: Hourly temporal series of the size segregated source apportionment fractions (VF = 0.85) for the fall SOAR ultrafine (UF), small accumulative mode (SAM), large accumulation mode (LAM), submicron (SUB), and supermicron (SUPER) particles using the updated source signature library. ....   | 250 |
| Figure 112: Representative 48 hour HYSPLIT back trajectories at a height of 100 m for six defined regions. (LA = Los Angeles, SD = San Diego).....   | 253 |
| Figure 113: Relative class abundance based on air mass origin and size range. (LA = Los Angeles, SD = San Diego, SS = Salton Sea, SJV = San Joaquin Valley, NE = Northeastern).....  | 254 |
| Figure 114: Size-resolved average area of secondary markers for particles matched to specific sources during the summer (left column) and fall (right column).....   | 256 |

## LIST OF TABLES

|   |     |
|---|-----|
| Table 1: The studies conducted as a part of this project. ....  | 2   |
| Table 2: Instrumentation. ....  | 15  |
| Table 3: Characteristics of ship plumes sampled including: Ship plume, plume peak time, plume duration, plume age, peak number concentration, identifying ATOFMS particle type, number of ATOFMS particles, number fraction of OC-V-sulfate particles, and number fraction of fresh soot particles. ....  | 31  |
| Table 4: Gas phase concentrations (max, baseline, and peak) of SO <sub>2</sub> , NO <sub>x</sub> , and Ozone during different plume events are shown along with the NO <sub>x</sub> /SO <sub>2</sub> ratio. ....  | 34  |
| Table 5: Sampling times and locations at sites around San Diego Bay are described. ....   | 48  |
| Table 6: Averages and standard deviations of ozone, ambient meteorological conditions, PM <sub>2.5</sub> mass concentrations (measured at the California Air Resources Board Rubidoux site), and PM <sub>1.0</sub> agedOC-nitrate-sulfate particle type mass concentrations for July 30 – August 15, 2005 compared to August 12, 2005 (189). ....   | 87  |
| Table 7: Measurements of PM <sub>2.5</sub> (µg/m <sup>3</sup> ), relative humidity (RH, %), temperature (T, °C), wind speed (WS, m/s), and gas-phase O <sub>3</sub> concentrations (ppb) for the sampling periods during 2005-2007. Standard deviations (σ) and measurement ranges are also listed. ‘Avg. Daily Maxima’ refers to the average time of the daily maximum of each particular factor. .... | 107 |
| Table 8: Descriptions of the major ATOFMS particle types from 2005-2007. ....   | 110 |
| Table 9: Correlation coefficients of PM <sub>2.5</sub> measurements. (a) Fresno site. (b) Angiola site. ....  | 135 |
| Table 10: APS scaling parameters for all studies. ....  | 142 |
| Table 11: Metal association percentages (%) ....  | 164 |
| Table 12: Properties of different regional events are listed including: peak PM <sub>1</sub> and PM <sub>2.5</sub> mass concentrations, fraction of PM <sub>1</sub> contributing to PM <sub>2.5</sub> mass, and the mass percentage of V-Ni-Fe and ECOC particles contributing to the PM <sub>1</sub> mass. ....  | 170 |
| Table 13: Overview of different Urey Hall CCN periods based on CCN activity, size distributions, particle chemistry and hysplit back trajectories (see dividing lines in figure 2). SMPS data is the average mode for that period with the min/max mode of dN/dlogD <sub>p</sub> in parenthesis. ....   | 185 |
| Table 14: Overview of SIO Pier CCN, fCCN, CN and Dact during Urey Hall CCN periods (from table 1a). ....  | 186 |
| Table 15: List of instrumentation. ....   | 194 |
| Table 16: List of Instrumentation used at the freeway and upwind sampling sites. ....   | 212 |
| Table 17: Number of library seeds for each source per size range ....   | 238 |
| Table 18: Percent difference between particles matched to the original source library and particles matches to the updated source library. ....   | 251 |

## ABSTRACT

In the past, the majority of research aimed at understanding the composition and sources contributing to  $PM_{2.5}$  concentrations in California has been focused on major field campaigns that have been concentrated over relatively short periods of time (weeks to months). While these studies have contributed a great deal to our understanding of aerosol particles, they have focused primarily on one region during one season. This report will detail the significant progress that has been made towards understanding how aerosol sources and chemistry vary temporally and spatially within California, information that is critical to assessing the health impacts of air pollution on individuals living in various regions of the state. The development of a trailer housing many air pollution instruments as a mobile platform for sampling has been a key enabling step in this research that has allowed for rapid deployment and the ability to sample in multiple locations over short periods of time. This increased flexibility has allowed us to obtain detailed information regarding the variations of aerosol properties both seasonally and spatially. The variations in particle concentrations and chemistry over very short time periods have allowed us to investigate changes in plumes from both roadways and ship traffic. In addition to changes in particles over different intervals of time, studies were conducted to investigate the changes in aerosol particle properties within a city scale range over the period of one air mass (3 days) and one day. Observations were also made of particle transport within California both locally (city-scale) and regionally (city-to-city). The second focus of this project has been to provide more detailed mass concentrations from aerosol time-of-flight mass spectrometry (ATOFMS) data, which has been achieved through scaling with respect to standard mass based measurements such as the MOUDI and TEOM. Advances have also been made in our ability to apportion individual particles to different sources building on a library of source signatures that has been developed through work with CARB over the last decade. Specifically, measuring changes in particle properties as they age and take up secondary material and the impact on the original source signatures has been investigated through the use of a thermodenuder, which has led to improved source apportionment capabilities of aerosols in highly aged environments.

## EXECUTIVE SUMMARY

### *Background*

Many studies have detailed the human health and environmental impacts of atmospheric aerosols since the middle of the 20<sup>th</sup> century. The majority of studies that have investigated particulate matter in the California atmosphere have been over relatively short time periods with a strong regional focus. These studies have provided a much greater understanding of aerosol particle physical properties and composition; however the majority of these studies have focused on bulk measurements that limit their ability to perform source apportionment. Bulk measurements are also challenged by positive and negative sampling artifacts and poor time resolution. In order to complement traditional sampling methods while overcoming some of the issues associated with off-line sampling, a number of techniques are being developed and used for real-time PM composition analysis. Single Particle Mass Spectrometry (SPMS) offers complementary information to bulk sampling by determining the actual chemical associations or mixing state of individual particles. SPMS techniques measure the size and chemical composition of individual particles and offer an alternative approach for performing source apportionment of ambient PM. Aerosol time-of-flight mass spectrometry or ATOFMS is the specific SPMS instrument used throughout this project. The strength of ATOFMS lies in its ability to provide information on the number fractions of particles with a specific chemical signature and how these vary with aerodynamic size. Unique associations within individual particles can be measured between organic carbon, elemental carbon, amines, nitrate, sulfate, ammonium, and metals. A major goal of ambient studies performed using ATOFMS involves linking specific single particle chemical signatures with specific emission sources, as well as developing a more quantitative picture of the fraction of secondary species associated with aerosols in polluted air under a variety of conditions and locations. In an effort to understand the relative contributions from different sources in California, we have begun using ATOFMS to perform extensive source characterization studies, characterizing the emissions from heavy duty diesel trucks and gasoline passenger cars, wildfires, wood smoke from fireplaces, meat cooking, and ships in an effort to determine differences in single particle mass spectral fingerprints from these sources. The ultimate goal is to develop single particle mass spectral signature libraries for major PM sources that can be compared to ambient particle spectra to assign sources and assess the rate and degree of aging that occurs on ambient PM over time and space.

### *Methods*

A wide range of gas and particle phase instruments were used in this study. Measurements of particle size distributions, PM<sub>2.5</sub> mass concentration, gas phase, black carbon concentrations, and single particle mass spectrometry were used in this project. The key unique instrument used for these studies was an aerosol time-of-flight mass spectrometer (ATOFMS), which analyzes individual particle size and composition in real time. Data from the ATOFMS was analyzed and incorporated into a mass spectral source library developed as a part of this project. The other gas and particle phase

instrumentation operated in the mobile trailer system included SO<sub>2</sub>, NO<sub>x</sub>, O<sub>3</sub>, CO, scanning mobility particle sizer (SMPS), aerodynamic particle sizer (APS), condensation particle counter (CPC), cloud condensation nuclei counter (CCN), aethalometer, and TEOM. A trailer was modified and combined with low particle emission generators to provide flexibility with respect to sampling location and duration with the suite of instrumentation listed above.

## ***Results and Conclusions***

This project was highly productive and accomplished a wide range of objectives including: high time resolution sampling, high spatial resolution sampling, seasonal and interannual comparisons, scaling and mass comparisons, changes in size-resolved particle composition linked with meteorological measurements and air mass back trajectories, and the development of source apportionment algorithms. High time resolution sampling led to the observation of ambient ultrafine aerosols by single particle techniques from both vehicle exhaust and photochemical events. It also allowed for the observation of individual ship plumes (~ 10-15 min in duration) and dramatic shifts in chemistry within them. Measurements looking at the spatial variability of aerosols were conducted in Riverside by comparing ATOFMS measurements at a stationary site with those made in the mobile laboratory during a Santa Ana period. Spatial analysis was also performed during a series of measurements made around San Diego Bay on days with different meteorological and aerosol characteristics. Seasonal variations were observed between SOAR I and SOAR II and led to analysis of diurnal variations (SOAR I) and episodic variations (SOAR II). Seasonal variations were also analyzed with respect to particle phase amines, as well as the ultrafine aerosols mentioned above. Interannual comparisons were also made for measurements made in Riverside during 2005, 2006, and 2007. Mass comparisons were made with TEOM, MOUDI, and BAM measurements allowing for the scaling of ATOFMS by APS data to quantitative mass concentrations. In depth analysis of the variation in APS scaling functions over numerous studies was investigated to refine the method. The link between meteorology measurements and air mass back trajectories were shown within the LA Basin with respect to trace metals. This link was also demonstrated regionally by showing the impact of the LA Port Region on San Diego air quality and its potential to significantly contribute to particle mass concentrations. Lastly, with respect to the development of source apportionment algorithms, mass spectral source signatures were used to apportion exhaust particles from gasoline and diesel powered vehicles in a freeway study. Source apportionment of PM<sub>2.5</sub> was also performed at that site for all particles, including non-vehicle sources. The source library that was developed was then used to characterize PM<sub>2.5</sub> in Athens, Greece and Mexico City, showing the broad applicability of the source library method. The library was also updated to include aging effects on source apportionment and to evaluate the aged Riverside environment.

# **Body of Report**

## **I. Introduction**

### **1. Research Objectives and Studies Conducted**

This project focused on using gas and particle phase instrumentation to analyze temporal and spatial variations as well as perform source apportionment of ambient aerosols in multiple regions of California. The project was divided into two phases and the major goals of Phase I were developing a mobile laboratory, acquiring and testing generators, conducting one field study in summer 2005, and performing source apportionment on previous ATOFMS source testing. The goals of Phase 2 (year 1) included combining the generators and mobile laboratory to allow for autonomous sampling, sampling during multiple seasons in multiple regions, and analyzing the data. Phase 2 (year 2) included additional sampling periods, analyzing all collected data, expanding data analysis techniques, and preparing a final report.

The sampling periods that were conducted as a part of this study are shown in table 1. The major studies were the Study of Organic Aerosols in Riverside (SOAR) I, SOAR II, SOAR III, SD Mobile Study, Pier Study, Los Angeles Basin Mobile Study (LABMS) I, LABMS II. The goals of the SOARs were to characterize the size and chemical composition of individual particles, provide quantitative information on different chemical compositions, study how aging processes affect fresh emission signatures determine the fraction of aged aerosol versus fresh aerosol, compare with other organic aerosol techniques including the AMS (Jimenez), thermal desorption MS (Ziemann), EC/OC measurements (Schauer), and SVOC measurements (Eatough), and identify the sources of Riverside aerosols and determine the fraction of fresh versus aged aerosols. The SD Mobile Study was the initial testing of the mobile laboratory powered by the generators, with the main goal being to determine and refine the mobile laboratory's capabilities. The Pier Study at Scripps Pier in La Jolla was partially funded as a collaboration with Prof. Mark Thiemens (1<sup>st</sup> 2 weeks), but was continued as part of this project to provide longer term sampling (last 5 weeks). The LABMS studies consisted of sampling in Long Beach and Riverside, with mobile sampling (1-2 sites per day) during LABMS II in the eastern half of the LA basin.

| Year | Study Name      | Location              | Months           | Season       |
|------|-----------------|-----------------------|------------------|--------------|
| 2005 | SOAR I          | Riverside             | July-August      | Summer       |
| 2005 | SOAR II         | Riverside             | November         | Fall         |
| 2006 | SOAR III        | Riverside             | August           | Summer       |
| 2006 | Pier Study      | San Diego             | August-September | Fall (early) |
| 2006 | SD Mobile Study | San Diego             | December         | Winter       |
| 2007 | LABMS I         | Long Beach, Riverside | August-September | Summer       |
| 2007 | SD Fires        | San Diego             | October-November | Fall         |
| 2007 | LABMS II        | Riverside, Long Beach | November         | Fall         |

**Table 1:** A list of the studies conducted as a part of this project.

## 2. Instrumentation

The principal sampling technique for ambient particles used throughout this report is aerosol time-of-flight mass spectrometry (ATOFMS). ATOFMS simultaneously acquires positive and negative ion spectra, as well as size information, for single particles in real-time. A detailed description of operation and performance of the transportable version of this instrument has been provided previously (1), though a brief explanation is included here. A schematic diagram of the standard inlet ATOFMS is given in **Figure 1**. The inlet region consists of a converging nozzle, followed by two skimmers. Similar to the APS, the particles undergo supersonic expansion upon introduction into vacuum and are accelerated to velocities dependent on their aerodynamic sizes. The different regions separated by skimmers fulfill two primary functions: to permit differential pumping from atmospheric pressures to the pressures necessary to operate the mass spectrometer and to collimate the particle beam by removing those particles which do not follow a straight trajectory. The particle beam next enters the light-scattering region, which includes two continuous-wave 532 nm diode pumped Nd:YAG lasers. These lasers are positioned orthogonally to the particle beam, so that when a particle passes through the laser beam, its scattered light is focused onto PMTs by means of ellipsoidal mirrors. The PMTs send pulses to an electronic timing circuit that measures the time the particle takes to travel the known distance (6 cm) between the two laser beams. The velocity of the particle is calculated with the particle time of flight and the distance and is converted to a physical aerodynamic diameter via an external size calibration with particles of known size. With the determined particle velocity, the timing circuit counts down to when the tracked particle will reach the center of the ion source region of the mass spectrometer and sends a signal to a pulsed Nd:YAG laser (frequency quadrupled to 266 nm) to fire. Through direct laser desorption/ionization (LDI), the laser pulse produces ions, which are then mass analyzed in a dual-ion reflectron time-of-flight mass spectrometer. The dual polarity permits simultaneous acquisition of positive and negative ion spectra for an individual particle, which is unique as most SPMS techniques can only obtain spectra of single polarity at a given time. The standard ATOFMS instrument can analyze single particles with aerodynamic diameters over a broad size range from approximately 200 to 3000 nm.

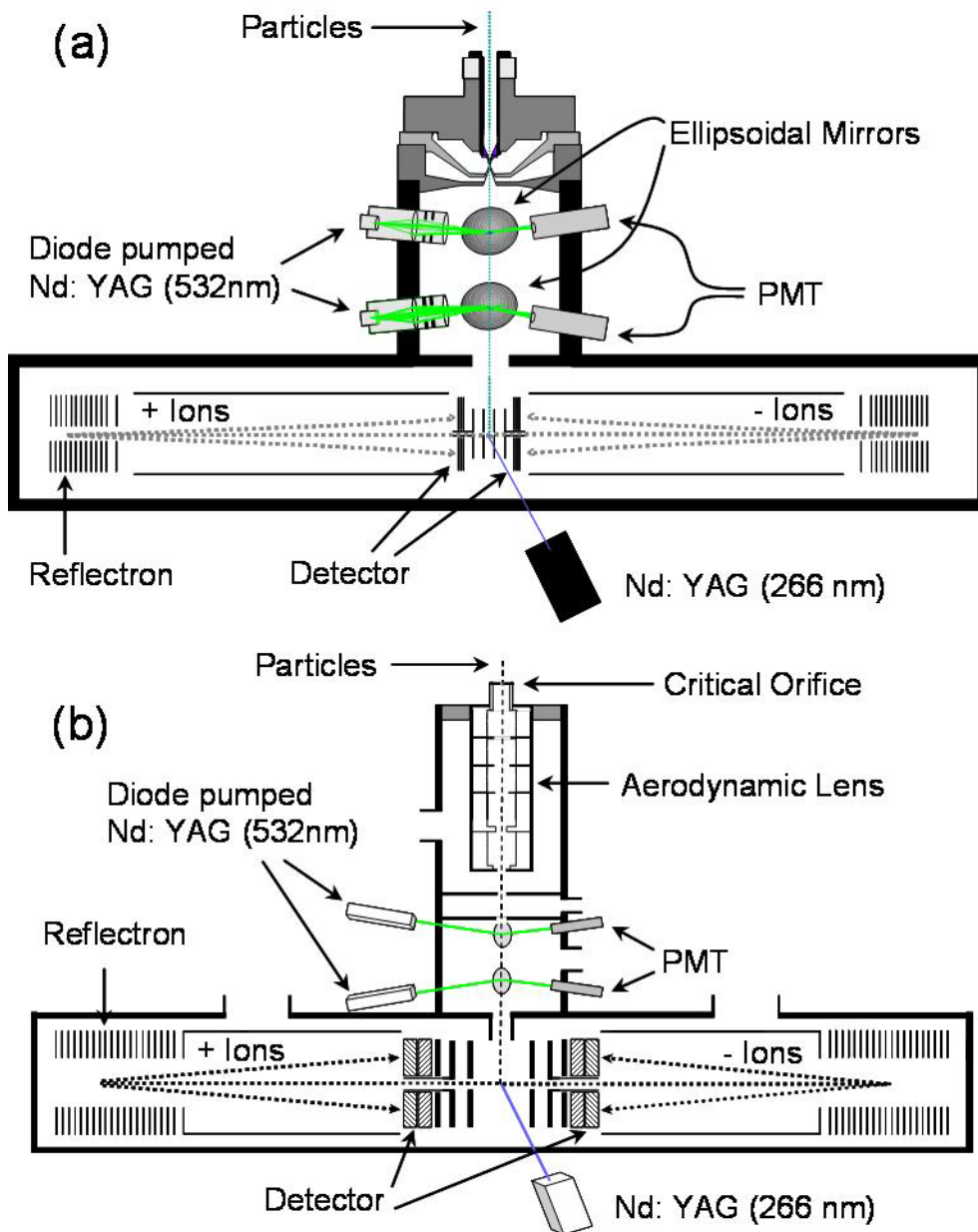


Figure 1: Instrument schematic diagrams of the (a) ATOFMS and (b) UF-ATOFMS.

Ultrafine aerosol time-of-flight mass spectrometry (UF-ATOFMS) has improved detection efficiency for small particles ( $< 300$  nm) over the standard ATOFMS by replacing the converging nozzle inlet with an aerodynamic lens inlet (2). **Figure 1b** shows the schematic diagram of the UF-ATOFMS instrument. The lens system tightly collimates the particle beam, so that smaller ultrafine particles will be more efficiently transmitted in the instrument (3,4). Upon exiting the aerodynamic lens, the gas molecules undergo supersonic expansion, accelerating the particles to terminal velocities based on their aerodynamic diameter – just as with standard inlet ATOFMS. UF-ATOFMS also has enhanced light-scattering detection by incorporating a focusing lens to tighten the continuous laser beams, increasing the laser beam power density, and by employing a fast amplifier to improve the signal-to-noise ratio. All of these



enhancements, in addition to the aerodynamic lens systems, are necessary to improve the minimum optical detection size of ~100 nm down to 50 nm. Together, standard ATOFMS and UF-ATOFMS cover an aerodynamic size range of ~50 to 3000 nm when sampling side-by-side.

### 3. Data Analysis Methods

ATOFMS generates large quantities of data; the instrumentation is capable of collecting size and chemical information on greater than 500 individual particles per minute, depending upon the atmospheric concentrations. While simple laboratory experiments may run for only a few hours, ambient monitoring studies with ATOFMS may operate for weeks. Therefore, continuous sampling during a single ambient study can yield tens of millions of individual spectra – far too many to analyze by hand. For efficient analysis of such a volume of data, an ideal data analysis technique must perform automatic sorting and classification of individual particles. There are a number of available mathematical algorithms that have been adapted to cluster mass spectral data, such as fuzzy *c*-means clustering, *k*-means clustering, hierarchical clustering, and artificial neural networks (5-9). The two main data analysis methods used in this report are described in the next sections. Any adjustments to these methods or alternative approaches will be discussed in subsequent chapters. The adaptive resonance theory-based neural network algorithm, ART-2a, has been used to analyze ATOFMS data for several years. In a benchmark test against other clustering methods, ART-2a has been shown to yield comparable results (8). A modification of ART-2a analysis involves matching to predefined seeds, such as a source signature library described below.

Though more detailed descriptions of the ART-2a algorithm have been provided elsewhere (10-12), a brief description is included here. Using the mass spectral ion patterns and peak intensities, ART-2a separates particles into distinct classes (clusters) of chemically similar particles within large ATOFMS data sets and generates new clusters whenever a data point (mass spectrum) falls outside the proximity to all existing classes. Thereby, ART-2a provides the advantage of determining the contributions from previously detected particle classes while also introducing information on new particle types. For each particle, ART-2a combines all of the ion peak patterns and intensities in the positive and negative spectra to form an *n*-dimensional weight vector (normally 350 *m/z* units for each polarity, making 700 units total), in which the ion intensity at each *m/z* ratio is normalized with respect to the maximum peak intensity present in the vector. In the classification process, particles are selected randomly and their spectral information is compared to each particle cluster (weight vector) by calculating the dot product of the particle vector and cluster weight vector. The dot product value ranges from 0 to 1, where 1 represents identical vectors. If the dot product value between the particle vector and any of the existing weight vectors is above the user-defined threshold (vigilance factor - VF), that particle is added to the cluster with the highest dot product value. If a learning rate is defined, that cluster will slightly weight its vector toward the newly added particle. If the dot product value is below the VF, the particle defines a new cluster. Once all of the particles have been assigned, ART-2a then compares each particle against the entire set of created clusters to ensure proper placement. This final step is repeated for a number of set iterations (usually 20).

Upon completion of the ART-2a analysis, there may be hundreds to thousands of resulting clusters based on the complexity of the data and the VF used. For example, a low VF ( $\leq 0.5$ ) will yield a low number of clusters with limited homogeneity, whereas a high VF ( $\geq 0.7$ ) will yield a large number of clusters with high homogeneity. The user then visually inspects the ART-2a clusters to manually classify and label them based on their spectral characteristics. Some clusters may be combined by hand if they have similar spectral characteristics or key class features, in order to reduce the total number of clusters to a more manageable size.

One of the features of ART-2a is that it can compare the ambient particle vectors to a set of predefined weight vectors, known as seeds. In direct analogy to the procedure described in the previous section, the dot product of each particle vector is crossed with each seed weight vector. The particle is placed into the seed cluster that produces the highest dot product, assuming it is above the user-defined VF. The main difference between this matching method and the normal ART-2a procedure is that if no dot product value exceeds the VF, the particle is placed into an “unmatched” category, rather than initiating a new particle class. In addition, this method has no learning rate parameter, so the vectors of the seeds remain constant as particles are matched to them.

The matching function is ideal for apportioning individual ambient particles to specific sources using a source signature library. The recently developed source signature library is described in detail elsewhere (13), but a brief description is given here. The size-segregated library combines the carefully identified mass spectral source signatures from a series of source (such as vehicle dynamometer studies) and ambient characterization studies to serve as the predefined cluster seeds. Designed to expand as the ATOFMS signatures for particles from new sources are obtained, the library presently contains source fingerprints for heavy duty diesel vehicle (HDDV) and light duty gasoline vehicle (LDV) exhaust emissions, dust, sea salt, biomass, and meat cooking. It also has non-source specific signatures acquired in ambient studies, including aged elemental carbon (EC), aged organic carbon (OC), amine-containing particles, ammonium-rich particles, vanadium-rich particles, EC, and polycyclic aromatic hydrocarbon (PAH)-containing particles. The major advantages of using this data analysis technique are the elimination of user bias in labeling and the speed in which it can apportion particles.

## **4. Summary of Chapters**

### **i. Introduction**

Chapter 0 introduces the goals of the project and motivation behind them, as well as the objectives and deliverables provided within the report. The aerosol time-of-flight mass spectrometer is then introduced as well as the trailer that was developed to transport it during this project. Previously developed as well as novel data analysis techniques are then described. Lastly, a brief summary of each chapter of the report is included.

### **ii. Time and Size Resolved Chemical Composition Measurements Detailing Short Term Changes in Composition**

Chapter 1 discusses the significant and largely unregulated presence of ultrafine particles in the atmosphere. Understanding the formation and sources of ambient

ultrafine particles represents a major goal, but analyzing such small particles is a considerable analytical challenge. This study demonstrates how real-time measurements of particle size and chemistry, coupled with gas-phase measurements, can provide unique insight into the daily and seasonal variations of the sources and chemistry of ultrafine particles. Measurements of ambient ultrafine particles are compared from three different single particle techniques which provide high temporal resolution during the 2005 summer (August) and fall (November) seasons in Riverside, CA in conjunction with the Study of Organic Aerosols at Riverside (SOAR) field campaign. During both seasons, vehicle exhaust emissions strongly contributed to the ultrafine particle concentrations during the weekday morning rush hour periods. SMPS measurements during the summer season showed high ultrafine particle concentrations during the afternoons most likely formed by photochemical events. In this study, different sources (and hence chemistry) contributed to the particles during periods of high ultrafine particle concentrations. Therefore, it is important to obtain simultaneous information on ultrafine particle sources as well as concentrations and advance beyond relying just on ultrafine particle concentrations as a proxy in future studies on health effects.

Chapter 2 investigates ship emissions, as they contribute significantly to gaseous and particulate pollution worldwide. To understand the impacts of ship emissions on human health and climate, the chemistry of the emitted particles must be well characterized. Therefore, the size-resolved chemistry distributions of individual particles in ship emissions were measured at the Port of Los Angeles using real-time, single-particle mass spectrometry. Ship plumes were identified through a combination of ship position information and measurements of gases and aerosol particles at a site 500 meters from the center of the main shipping channel of the Port of Los Angeles. Particles containing organic carbon, vanadium, and sulfate (OC-V-sulfate) resulted from residual fuel combustion (i.e. bunker fuel), whereas high quantities of fresh soot particles (when OC-V-sulfate particles were not present) represented distinct markers of plumes from distillate fuel combustion (i.e. diesel fuel) from ships as well as trucks in the port area. OC-V-sulfate particles from residual fuel combustion had significantly higher levels of sulfate and sulfuric acid than plume particles containing no vanadium. We hypothesize that these associations are due to the vanadium (or other metals such as iron or manganese) in the fuel catalyzing the oxidation of  $\text{SO}_2$  to produce sulfate and sulfuric acid on these particles. This has been shown previously in laboratory studies to occur at ambient temperatures ( $> 25^\circ\text{C}$ ) in the presence of  $\text{H}_2\text{O}$  and  $\text{NO}_2$  (both present in ship plumes), but these results using single particle mixing state mark the first direct observation of this process under freshly emitted ambient conditions. Enhanced sulfate production on V-containing ship emission particles may lead to the measured levels of sulfate in California, which are currently higher than expected based on emissions inventories. Understanding the overall impact of ships emissions is critical for controlling regional air quality in coastal regions of the world.

### **iii. Spatial Variability of Particulate Matter and Sources**

Chapter 3 describes how understanding the spatial and temporal variability of particle concentrations and chemistry within the urban aerosol is critical to determining exposure levels and the impact on human health. However, it is difficult to accurately determine this variation by measurements or modeling over small distances with high

time resolution, such as a neighborhood scale of a few kilometers over a few hours. This challenge often leads to simplifications in how models treat the urban aerosol that are not always indicative of ambient conditions. To gain a better understanding of how particle size and chemistry changes on a neighborhood scale within the urban aerosol, the mobile aerosol time-of-flight mass spectrometry (ATOFMS) laboratory was deployed to 3-5 sites over a roughly 10 km<sup>2</sup> area on two days (3 sites on February 12, 2009 and 5 sites on March 13, 2009). ATOFMS measurements of size-resolved single-particle chemical composition (0.2 – 3.0 µm) in conjunction with aerosol mass concentration below 2.5 micrometers (PM<sub>2.5</sub>) and size-resolved number concentration measurements provided a detailed characterization of the urban aerosol with high time resolution. Particle concentrations and chemistry were found to differ significantly on these two days, which were characterized by similar meteorological conditions and gas phase concentrations (SO<sub>2</sub>, NO<sub>x</sub>, and O<sub>3</sub>). Clean conditions following rain, observed on the first day of sampling were characterized by low mass and number concentrations with similar chemistry observed across all sites, suggesting decreased influence of local sources. However, during sampling on the second day under more polluted conditions, substantial variation in particle mass, number, and chemistry particularly in the accumulation mode (0.2-1.0 µm), were observed at the various sites around the bay. For the high PM<sub>2.5</sub> concentration day, decreases in the mass fraction of organic carbon particles and decreases in nitrate on background particle types during the day followed a diurnal pattern. Thus, while minor particle variations were observed spatially on this second day, temporal trends played a greater role in controlling variation in particle concentration and chemistry. These results indicate that strengthening the link between particles and human health requires a more detailed understanding of temporal variations of single particle mixing state within the urban aerosol that PM<sub>2.5</sub> mass concentrations alone cannot provide.

#### **iv. Seasonal and Interannual Variability in Particulate Matter Size and Composition**

Chapter 4 details aerosol time-of-flight mass spectrometry (ATOFMS) measurements that were conducted during the Study of Organic Aerosols in Riverside, California (SOAR) field campaign in the summer and fall of 2005. Time and size-resolved number fractions of the major particle types are presented for the size range of 0.2–2.5 µm. In general, carbonaceous particles which were mixed with nitrate, sulfate and ammonium dominated (>75%) the aerosols below 1.0 µm, and aged sea salt, dust and aged carbonaceous particles were the major particle types above 1.0 µm, except during the fall Santa Ana periods when dust and biomass particles were prevalent over the whole size range. Most of the major particle types during the summer displayed strong diurnal variations, with high carbonaceous number fractions appearing from night until the morning and aged sea salt, dust, biomass, and OC-vanadium particles peaking in the afternoon. In contrast, fall measurements showed distinct episodic events dominated by different particle types. The majority of the ambient particles contained secondary nitrate and sulfate with higher amounts of particle phase sulfate in the summer and nitrate in the fall. In both seasons, the beta attenuation monitor measurements displayed similar temporal trends when compared to the ATOFMS total carbonaceous fractions, indicating

that carbonaceous particles mixed with sulfate, nitrate, and ammonium were the major component of the PM<sub>2.5</sub> mass concentrations.

Chapter 5 describes how, during the summer and fall of 2005 in Riverside, California, the seasonal volatility behavior of submicrometer aerosol particles was investigated by coupling an automated thermodenuder system to an online single-particle mass spectrometer. A strong seasonal dependence was observed for the gas/particle partitioning of alkylamines within individual ambient submicrometer aged organic carbon particles internally mixed with ammonium, nitrate, and sulfate. In the summer, the amines were strongly correlated with nitrate and sulfate, suggesting the presence of aminium nitrate and sulfate salts which were nonvolatile and comprised ~6-9% of the average particle mass at 230 °C. In the fall,  $86 \pm 1\%$  of the amines volatilized below 113 °C with aminium nitrate and sulfate salts representing less than 1% of the particle mass at 230 °C. In the summer, a more acidic particle core led to protonation of the amines and subsequent formation of aminium sulfate and nitrate salts; whereas, in the fall, the particles contained more ammonium and thus were less acidic, causing fewer aminium salts to form. Therefore, the acidity of individual particles can greatly affect gas/particle partitioning of organic species in the atmosphere, and the concentrations of amines, as strong bases, should be included in estimations of aerosol pH.

Chapter 6 discusses how to date most single-particle mixing state studies have focused on individual intensive field studies to draw conclusions about health-related impacts of aerosols. Health and pollution models develop parameters based on these studies and do not incorporate how particle characteristics can change on a yearly basis. Inter-annual variability of ambient particle characteristics was observed using single-particle mass spectrometry during three consecutive summer studies in Riverside, CA. Single-particle mixing states with secondary species and PM<sub>2.5</sub> mass concentrations were found to vary with meteorology. These inter-annual variations can be used to optimize parameters in health models such that input parameters representing different meteorological conditions each year could improve the predicted particle chemistry and concentrations and improve pollution regulations. For instance, 2005 represented a consistently diurnal year with an aged organic atmosphere, 2006 was a cool, moist year correlating with an amine-rich environment, and 2007 was a Santa Ana year correlating to the presence of dust and salts. Although the particle chemistry was different each year, particles containing elemental carbon internally mixed with organic carbon had similar temporal trends to PM<sub>2.5</sub> mass concentrations, comprising 13-31% of the total number of particles. This suggests a large influence of aged anthropogenic particles on particle mass; however, this pattern was not constantly observed because of the large presence of other types mentioned above. In the future, these results could be used as a first approximation as to what the detailed chemical composition of PM<sub>2.5</sub> may be given a set of meteorological conditions, which is what many health standards are based on. Since continuous intensive particle measurements are difficult long-term, the chemistry indicated by meteorological conditions can be used in models to predict how PM<sub>2.5</sub> changes impact human health.

## **v. Mass Comparisons and Investigations into the Volatile and Semivolatile Fraction of Particles**

Chapter 7 shows a comparison of two approaches for converting unscaled ATOFMS measurements into quantitative particle mass concentrations using (1) reference mass concentrations from a co-located micro-orifice uniform deposit impactor (MOUDI) with an accurate estimate of instrument busy time, and (2) reference number concentrations from a co-located aerodynamic particle sizer (APS). Aerodynamic-diameter-dependent scaling factors are used for both methods to account for particle transmission efficiencies through the ATOFMS inlet. Scaling with APS data retains the high-resolution characteristics of the ambient aerosol because the scaling functions are specific for each hourly time period and account for a maximum in the ATOFMS transmission efficiency curve for larger sized particles. Scaled mass concentrations obtained from both methods are compared with co-located PM<sub>2.5</sub> measurements for evaluation purposes. When compared against mass concentrations from a beta attenuation monitor (BAM), the MOUDI scaled ATOFMS mass concentrations show correlations of 0.79 at Fresno, and 0.91 for the APS scaled results at Angiola. Applying composition dependent density corrections leads to a slope of nearly one with zero intercept between the APS scaled absolute mass concentration values and BAM mass measurements. This paper provides details on the methodologies used to convert ATOFMS data into continuous, quantitative, and size resolved mass concentrations that will ultimately be used to provide a quantitative estimate of the number and mass concentrations of particles from different sources.

Chapter 8 provide greater detail on the challenges of scaling ATOFMS data with the aerodynamic particle sizer (APS). Quantitative mass concentrations of different particle types can be obtained by scaling the ATOFMS data with aerodynamic particle sizer (APS) number concentration measurements. A question arises as to the stability of this procedure in multiple field locations. In this study, the effect of correcting ATOFMS measurements of two studies in Fresno and Angiola with APS scaling functions from different reference field studies conducted in other locations was investigated. Notably, the particle type mass fractions obtained within the submicron ( $0.3 \leq D_a < 1.0 \mu\text{m}$ ) size range were almost identical, regardless of the reference APS scaling function used. More differences (0.089% - 15%) were obtained in the supermicron ( $1.0 \leq D_a \leq 2.5 \mu\text{m}$ ) mass fractions, mainly due to the shift in the minima of scaling curves at higher sizes. Higher mass fractions (~5% more) of aged sea salt particles and lower fractions of carbonaceous particles were obtained when scaling supermicron particles of object studies with the APS scaling functions from APMEX and NC-CCS-II studies. No substantial differences were observed when scaling the specific studies with either the co-located or reference scaling functions. Therefore, this study demonstrates that an estimate of the submicron particle type mass fractions within 10 % and of supermicron particle type mass fractions within 19% can be obtained by scaling ATOFMS measurements with APS scaling functions from other studies if no co-located APS measurements are available.

## **vi. Changes in the Size-Resolved Particle Composition Linked with Meteorological Measurements and Air Mass Back Trajectories to Increase Understanding of Sources and Secondary Contributions to Particulate Matter**

Chapter 9 discusses that trace metal-containing particulate matter (PM) has been associated with health effects and environmental contamination despite representing only a small mass fraction of ambient PM. Using aerosol time-of-flight mass spectrometry (ATOFMS), individual particles with sizes ranging from 100-2550 nm were examined during the 2005 summer and fall seasons in Riverside, California for the following trace metals: V, Fe, Ni, Cu, Zn, Sr, Mo, Sn, Sb, Ba, W, and Pb. The chemical speciation, temporal trends, seasonal differences, size distributions, and wind direction dependencies are reported for the five trace metals (V, Fe, Zn, Ba, and Pb) that exhibited the highest number concentrations. By combining this information, the potential sources of the trace metal-containing particles can be identified, whether they are local or from long-range transport. The metal-containing particles demonstrated different temporal and spatial trends in the summer versus the fall; both Ba and Pb particles were found to be more abundant during the fall due to their source locations and the wind direction. Many of the particle classes are identified as originating from anthropogenic sources (industrial and transport sector) in the Los Angeles Basin.

Chapter 10 shows that ship and other emissions near the Los Angeles and Long Beach Port region strongly influence air pollution levels in the San Diego area. During time periods with regional transport, atmospheric aerosol measurements in La Jolla, California show an increase in 0.5-1  $\mu\text{m}$  sized single particles with unique signatures including soot, metals (i.e. vanadium, iron, and nickel), sulfate, and nitrate. These particles are attributed to primary emissions from residual oil sources such as ships and refineries, as well as traffic in the port region, and secondary processing during transport. During regional transport events, particulate matter concentrations were 2-4 times higher than typical average concentrations from local sources, indicating the health, environmental, and climate impacts from these emission sources must be taken into consideration in the San Diego region. Unless significant regulations are imposed on shipping-related activities, these emission sources will become even more important to California air quality as cars and truck emissions undergo further regulations and residual oil sources such as shipping continue to expand.

Chapter 11 discusses that during the 2007 wildfires in San Diego County over 2,000 homes and 300,000 acres of land were burned. For the duration of these fires, from October 21<sup>st</sup> through November 1<sup>st</sup>, 2007, individual particle size and composition along with total particle and cloud condensation nuclei (CCN) concentrations were measured in real-time at the University of California San Diego (UCSD) main campus and Scripps Institution of Oceanography Pier. Aerosol hygroscopicity was estimated from the CCN measurements and compared to the simultaneous aerosol chemistry and size distribution measurements. Near the beginning of the wildfires CCN concentrations were between 2,000 -14,000  $\text{cm}^{-3}$  and biomass burning aerosol (BBA) made up more than 80% of the total particles  $<300\text{nm}$ . The BBA produced by the wildfires made a dominant contribution to the CCN populations observed. The lower hygroscopicity parameter ( $\kappa$ ) range observed in this study for the UCSD campus ( $\kappa = 0.004\text{-}0.3$ ) indicates that there were non-hygroscopic or insoluble compounds present in the BBA. The biomass emissions measured during these wildfires were somewhat below, and on the lower end

of, the range of previously determined BBA hygroscopicities from both controlled burns and ambient measurements. The BBA during the beginning of the fires were relatively fresh and consisted primarily of KCl and water soluble organic compounds (WSOC) including formic and acetic acids and levoglucosan, measured using aerosol time-of-flight mass spectrometry (ATOFMS). As the BBA aged they contained increased amounts of  $\text{KHSO}_4$  compounds, and more oxidized organic compounds including oxalic acid. This was likely caused by a transition from flaming fires to predominantly smoldering fires, as well as increased atmospheric aging. Concurrent with these changes in particle chemistry, both the CCN concentration and particle hygroscopicity decreased. This indicates an important role of the inorganic component of the BBA in influencing the CCN population and particle hygroscopicity. A correlation between particle-phase ammonium and hygroscopicity during a particular event was also observed. The ammonium may have shifted the acid-base neutrality of the aerosols, possibly allowing additional weaker acids to partition to the aerosol phase.

### **vii. Development of Source Apportionment Algorithms**

Chapter 12 details how single particle mass spectrometry techniques such as aerosol time-of-flight mass spectrometry (ATOFMS) offer a unique approach for on-line source apportionment of ambient aerosols. Source signatures, or mass spectral "fingerprints", have been obtained using ATOFMS from a variety of sources with an emphasis placed on distinguishing between emissions from different types of vehicles. In this study, the signatures from previous source tests of diesel powered heavy duty vehicles (HDDV) and gasoline powered light duty vehicles (LDV) are matched to particle spectra acquired during a freeway-side study performed over a month in southern California to source apportion the particles. Using a relatively high matching (vigilance) factor of 0.85, particle mass spectral signatures from the vehicle source studies matched 83% of the freshly emitted particles detected alongside the freeway. The particle contributions alongside the freeway in the ultrafine and accumulation size range (aerodynamic diameter = 50–300nm) were apportioned to 32% LDV, 51% HDDV, and 17% from other sources. This paper discusses the apportionment process used and the methods used for validation with peripheral instrumentation.

Chapter 13 describes how several approaches for ambient aerosol source apportionment have been developed over the years. A number of these techniques involve determining organic and inorganic source markers from offline bulk filter analysis using a variety of analytical tools (such as mass spectrometry, chromatography, and microscopy). Some other methods have inferred that certain sources can be determined from correlations between particle size data and gas phase measurements. The technique presented here involves using a mass spectral source signature library to apportion single particles detected with an aerosol time-of-flight mass spectrometer (ATOFMS). The source signature library has been developed through a series of source and ambient characterization studies and currently contains signatures for heavy duty diesel vehicles (HDDV), light duty gasoline vehicles (LDV), dust, sea salt, biomass, and meat cooking. There are also additional non-source specific signatures, determined from the data acquired for several ambient ATOFMS studies, for aged organic carbon, aged elemental carbon, amine containing particles, PAH's, ammonia rich particles, vanadium particles, and elemental carbon particles. Using the ART-2a algorithm to match



individual ambient particle mass spectra to the source signature library, it was found that 97% of ambient particles (50 – 3000 nm) detected with two ATOFMS instruments near a freeway matched the library signatures. The use of the ART-2a source signature matching method shows that particles from gasoline powered vehicles can be readily distinguished from heavy duty diesel powered vehicles in roadside ambient measurements. Additionally, it was discovered that regional background particles matching with specific elemental carbon and vanadium signatures from ship emissions dominate and overwhelm the local emissions; however, the library matching method is able to identify their presence and distinguish them from local emissions.

Chapter 14 describes a new source apportionment method using a library composed of unique source mass spectral signatures obtained by aerosol time-of-flight mass spectrometry (ATOFMS) has been developed. The goal of this chapter is to apply this source signature library to an ambient dataset collected in a highly aged environment to evaluate the performance of the source apportionment method in a more aged environment and to determine the relative contributions of the major primary and secondary sources to the atmospheric aerosol. Ambient particles ranging in aerodynamic diameter from 50 to 3000 nm were analyzed in Riverside, California in conjunction with the Study of Organic Aerosols at Riverside (SOAR) campaign in the summer and fall seasons of 2005. The apportionment results showed that the majority of small (50-140 nm) ambient particles came from local vehicle exhaust emissions. The larger (140+ nm) particles demonstrated strong seasonal differences. Based on differences in meteorological conditions, the time series for the summer particles followed diurnal patterns, whereas the fall particles displayed episodic behavior. It was determined that the original source signature library did not apportion a significant number of particles; therefore, multiple approaches were explored and tested to improve the total number of particles detected in this challenging environment that were matched. It was found that introducing new seeds made from aged ambient particles to the library yielded better results than by lowering the “matching” or data analysis factor. By adding additional aged seeds to the source signature library, the unclassified category was reduced (as much as 14%) and the contribution of the aged particle types increased, thus improving the source apportionment method so it can now be used on ambient datasets collected in aged environments. In addition, the extent of aging of particles from primary sources was investigated focusing on secondary species including nitrates, sulfates, and amines. It was revealed that although nitrate has different seasonal sources, it is the dominant secondary species on aged particles from primary sources in Riverside.

Chapter 16 includes a summary and concluding remarks regarding the major findings presented in this report.

## II. Objectives and Results

### Time and Size Resolved Chemical Composition Detailing Short Term Changes in Composition

#### 1. Detection of ambient ultrafine aerosols by single particle techniques during the SOAR 2005 campaign

##### i. Introduction

High concentrations of atmospheric ultrafine particles (aerosols with diameters less than 100 nm) have been observed worldwide, from arctic areas and remote regions to coastal marine locations and urban environments (14). Growing evidence suggests that the inhalation of ultrafine particles may have more adverse health effects than larger particles has raised interest in the sources and atmospheric processing of these particles (15). Ambient particles can be divided into two basic categories based on their production mechanism: primary, which are directly emitted from sources such as vehicles and industrial processes, and secondary, which are formed via gas-to-particle conversions (16). The formation and growth of secondary ultrafine particles during nucleation events have been the focus of intensive research recently, leading to the proposal of several different formation mechanisms (14,17,18). From a regulation perspective, it is important to be able to distinguish the origin of the ultrafine particles, as primary and secondary particles require different means of control (direct emissions versus gaseous precursors).

The small size of ultrafine particles makes them much more challenging to detect than larger particles. Despite accounting for greater than 80% of the number of particles in  $PM_{2.5}$  (particulate matter with diameters less than 2.5  $\mu m$ ), estimates suggest that ultrafine particles collectively represent very little mass ( $< 20\%$ ) (16,19,20). Therefore,  $PM_{2.5}$  regulations based on mass concentrations do not provide a good control for the concentrations of ultrafine particles (21). The poor correlation between  $PM_{2.5}$  and ultrafine particles suggests that number-based measurements may be better suited for studying ultrafine particles than a bulk  $PM_{2.5}$  mass approach. Size-fractionated mass measurements by a NanoMOUDI (Nano-micro orifice uniform deposit impactor) have been obtained (22), but the continuous sampling time required to collect sufficient material for mass and chemical analysis can be as long as two weeks (23). With such long sampling periods, it is difficult to extract details about specific short-lived ultrafine particle episodes (19,21,24), which can be captured by high temporally-resolved continuous measurements. Techniques that rely on optical detection are problematic, because as the particle diameter becomes increasingly smaller than the wavelength of light, the intensity of the scattering signal quickly plummets; the minimum practical observable particle size using optical techniques commonly is  $\sim 100$  nm (25,26). Therefore, in order to efficiently detect ultrafine particles optically, it is necessary to enhance previously developed instrumentation. Several approaches have been tried

successfully, such as growing small particles into detectable sizes for counting via the condensation particle counter (CPC) (27) or by using specific critical orifices to create an upstream pressure that focuses particles of a given size range such as with the single particle mass spectrometer known as RSMS (28-30).

The main goals of this study involve comparing the seasonal variability of ultrafine particle concentrations in Riverside, CA from three different techniques with high temporal resolution and to use the combined data in conjunction with other peripheral instrumentation for deriving a better understanding of ultrafine particle chemistry. Riverside is located east of the Los Angeles (LA) Basin and, due to generally consistent meteorological patterns, is regularly downwind of the pollutants emitted in the LA area. The instruments used in this study include a scanning mobility particle sizer (SMPS), an ultrafine condensation particle counter (UF-CPC), and an ultrafine aerosol time-of-flight mass spectrometer (UF-ATOFMS). Supporting data from co-located gas- and particle-phase instruments, as well as meteorological measurements, are used to provide additional insight into the origin of the ultrafine particles.

## ii. Experimental

Sampling on the campus of the University of California, Riverside (33°58'18"N, 117°19'22"W) during the summer (July-August) and fall (October-November) of 2005 occurred in conjunction with the Study of Organic Aerosols at Riverside (SOAR) field campaign. Details on the sampling location and inlets of the mobile laboratory can be found elsewhere (31). **Table 2** provides the acronym, model, measurement, and sampling interval for each instrument used in this manuscript. All instrumentation, except for the CPCs and summer CO analyzer, were housed in a mobile laboratory; the other instruments were located in nearby trailers with similar sampling inlets (PM<sub>2.5</sub> inlet cutoffs and reflective insulation wrap on the sampling lines). Ambient temperature, relative humidity (RH), and photosynthetically active radiation (PAR) measurements were provided by the Goldstein group of the University of California, Berkeley. The work presented here focuses on one week of data collected in the summer (Sunday, August 7<sup>th</sup> through Saturday, August 13<sup>th</sup>) and fall (Sunday, November 6<sup>th</sup> through Saturday, November 12<sup>th</sup>) seasons. Though Santa Ana events, characterized by dry easterly winds, tend to occur during fall and winter months, they do

**Table 2: Instrumentation.**

| Instrument   | Make & Model                 | Measurement                                    | Averaging Interval |
|--|------------------------------|--|--------------------|
| Scanning Mobility Particle Sizer (SMPS)                        | TSI Model 3936L 10           | particle number concentration (15-866 nm)      | 5 min              |
| Ultrafine Condensation Particle Counter (UF-CPC)               | TSI Model 3025A              | particle number concentration (> 3 nm)         | 1 min              |
| Ultrafine Aerosol Time-of-Flight Mass Spectrometer (UF-ATOFMS) |                              | chemical composition (50-400 nm)               | real-time          |
| Aethalometer   | Magee Scientific AE-3 Series | optical absorption cross-section per unit mass | 5 min              |
| CO Analyzer (summer)   | TEI Model 48CTL              | CO concentration levels                        | 30 min             |
| CO Analyzer (fall)   | Ecotech EC 9830              | CO concentration levels                        | 1 min              |
| Chemiluminescence NO-NO <sub>2</sub> -NO <sub>x</sub> Analyzer | TEI Model 42C                | NO & NO <sub>x</sub> concentration levels      | 1 min              |
| UV Photometric O <sub>3</sub> Analyzer                         | TEI Model 49C                | O <sub>3</sub> concentration levels            | 1 min              |

TEI: Thermo Environmental Instruments

not represent the average fall conditions. Therefore, the representative fall week for this study does not contain any Santa Ana events (31). Results are presented in Pacific Standard Time (PST), which is one hour behind local time during the summer.

It is important to briefly review the main operating principles of each instrument in order to understand how the measurements are made and upon which aerosol properties they depend. In this study, ultrafine particles are defined as having diameters less than 100 nm; although, each of the techniques in this study use different size metrics. CPCs provide continuous real-time ambient number concentration measurements by optically counting particles upon which a vapor has condensed. The CPC effectively lowers the minimum size detection cutoff by enlarging the particle diameter by the use of a condensable vapor such as an alcohol (27). The butanol-based TSI 3025A UF-CPC has a minimum diameter cutoff of 3 nm. An SMPS measures the number-based particle size distributions based on their electrical mobility diameter through the combination of a differential mobility analyzer (DMA) connected to a CPC. By scanning through the set voltage range, a range of mobility diameters can be selected and counted. In this study, the SMPS used a TSI 3010 CPC with a TSI 3080 electrostatic classifier (DMA) and was set to have a lower mobility diameter limit of 15 nm. The UF-ATOFMS simultaneously acquires positive and negative ion mass spectra, as well as aerodynamic diameter information, for single particles in real-time. It has improved detection efficiency for small particles (<300 nm) over the standard transportable ATOFMS (1) by replacing the converging nozzle inlet with an aerodynamic lens inlet (2). The lens system tightly collimates the particle beam, so that smaller ultrafine particles will be more efficiently transmitted in the instrument (3,4). The UF-ATOFMS also has enhanced light-scattering detection by the use of focusing lens to tighten the continuous laser beams, increasing the laser beam power density, and by employing a fast amplifier to improve the signal-to-noise ratio (2). All these enhancements, in addition to the aerodynamic lens systems, are necessary to improve the minimum optical detection size of ~100 nm down to 50 nm. In this study, chemical information was obtained for approximately 20.5% and 28.6% of the ultrafine particles that were sized by the UF-ATOFMS during the summer and fall, respectively. Just like ambient particles of larger sizes, less than 100% of the particles that are sized produce mass spectra due to factors such as the interaction between the particle beam and the 266 nm laser beam, chemical composition, and desorption/ionization capability of the particle (2,32). The percentages of the ultrafine particles that were chemically analyzed fit well within the overall range (15-35%) of all

ambient particles chemically analyzed by the UF-ATOFMS throughout both studies. Most of the observed variability in the percentage of particles that were chemically analyzed could be explained by busy time issues, as previously discussed in Sodeman et al. [Sodeman et al., 2005]. During periods with very high particle concentrations (all sizes), the older data acquisition system used for this study was unable to save the spectra as quickly as they were produced, lowering the overall percentage of chemically analyzed particles.

The instruments detect particles based on their optical, electrical mobility, or aerodynamic diameters. The electrical mobility diameter of a particle is the diameter of a sphere with an identical migration velocity in a constant electric field (33), and the aerodynamic diameter of a particle is the diameter of a sphere of unit density with the same terminal velocity (26). DeCarlo and coworkers present a detailed theoretical review of the relationship between the electrical mobility and aerodynamic diameters of a particle (34). Briefly, both diameters are dependent upon the shape of the particle. With increasing irregularity, the mobility diameter increases, whereas the aerodynamic diameter decreases. As opposed to the electrical mobility diameter, the aerodynamic diameter also is governed by the density of the particle, increasing with higher particle densities. The particle density is mainly dictated by the chemical composition and shape of the particle. Spherical particles of unit density will have the same electrical mobility and aerodynamic diameters.

Among these instruments, only the UF-ATOFMS obtains chemical information in addition to the size of the single particles. The UF-ATOFMS chemically analyzed 16,321 ultrafine particles during the summer week-long period and 20,320 ultrafine particles during the fall period. In order to group the ultrafine particle (aerodynamic diameter 50-100 nm) mass spectra measured by the UF-ATOFMS into chemical classes, an adaptive resonance theory neural network algorithm (ART-2a) was employed. ART-2a sorts and categorizes individual particles into clusters based on similar mass spectral characteristics (35). The main user-defined parameters for ART-2a are the learning rate, number of iterations, and vigilance factor, which were set to 0.05, 20, and 0.80, respectively, for this work. The resulting most populated 50 clusters, which represent ~97% of the total sampled particles, were further combined by hand (based on chemical similarities) to yield the general classes presented herein.

### **iii. Results and discussion**

#### ***a. Ambient measurements***

The UF-ATOFMS measured the chemistry of individual ultrafine particles detected during the SOAR campaigns. **Figure 2** displays the hourly number of particles for which the UF-ATOFMS obtained both size and chemical information as a function of aerodynamic diameter between 50-400 nm. Upstream of the UF-ATOFMS, a modified micro-orifice uniform deposit impactor (MOUDI) decreased the transmission of larger particles so that the UF-ATOFMS had more opportunity to analyze the smaller particles, which are harder to detect due to their lower transmission efficiencies. The figure shows that the UF-ATOFMS primarily detected particles with aerodynamic diameters between 150 and 300 nm, which was due to a combination of the high ambient concentrations and instrument detection abilities. The top plot clearly shows that the number of detected ultrafine particles (50-100 nm) spiked each morning during weekday rush hour periods.

While the UF-ATOFMS measurements do not represent true counting statistics due to transmission efficiency issues (2), it does provide chemical information about the single particles it detects and the relative percentages of each type. The top mass spectra representing each of the general chemical classes are shown in **Figure 3**. **Figure 4** provides the relative size distributions of the particle types during both the summer and fall seasons and also shows the size dependence of the particles that are chemically analyzed by the UF-ATOFMS. The 50-60 nm bin has the least number of chemically analyzed particles (55 and 78 particles for summer and fall, respectively), because they are the smallest and, therefore, most difficult to detect. The top five particle types have carbon cluster peaks ( $C_1$ ,  $C_2$ ,  $C_3$ , etc.) indicative of elemental carbon (EC) and

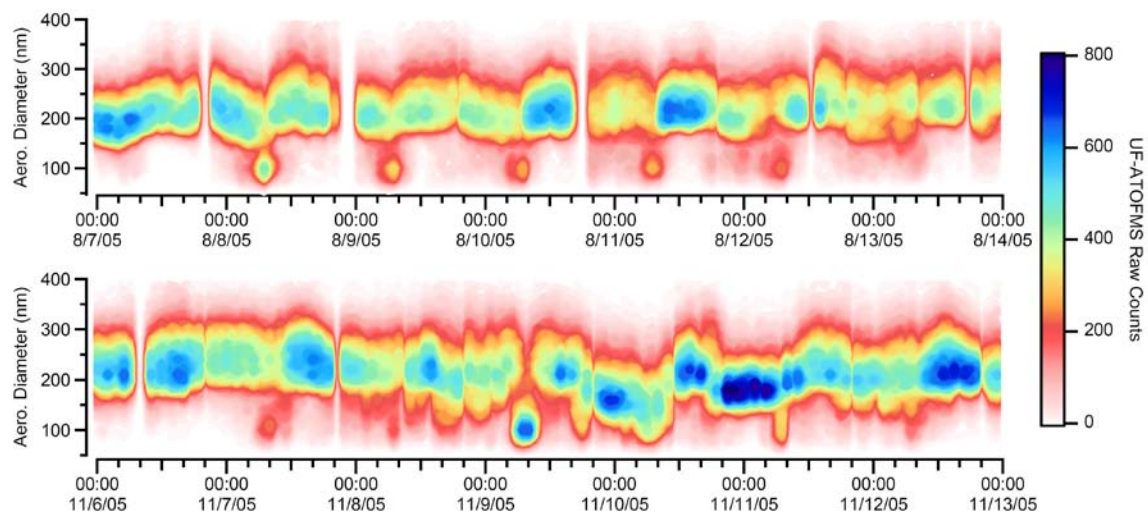


Figure 2: Hourly UF-ATOFMS counts of single particles for which chemical information was obtained as a function of aerodynamic diameter during the summer (top) and fall (bottom).

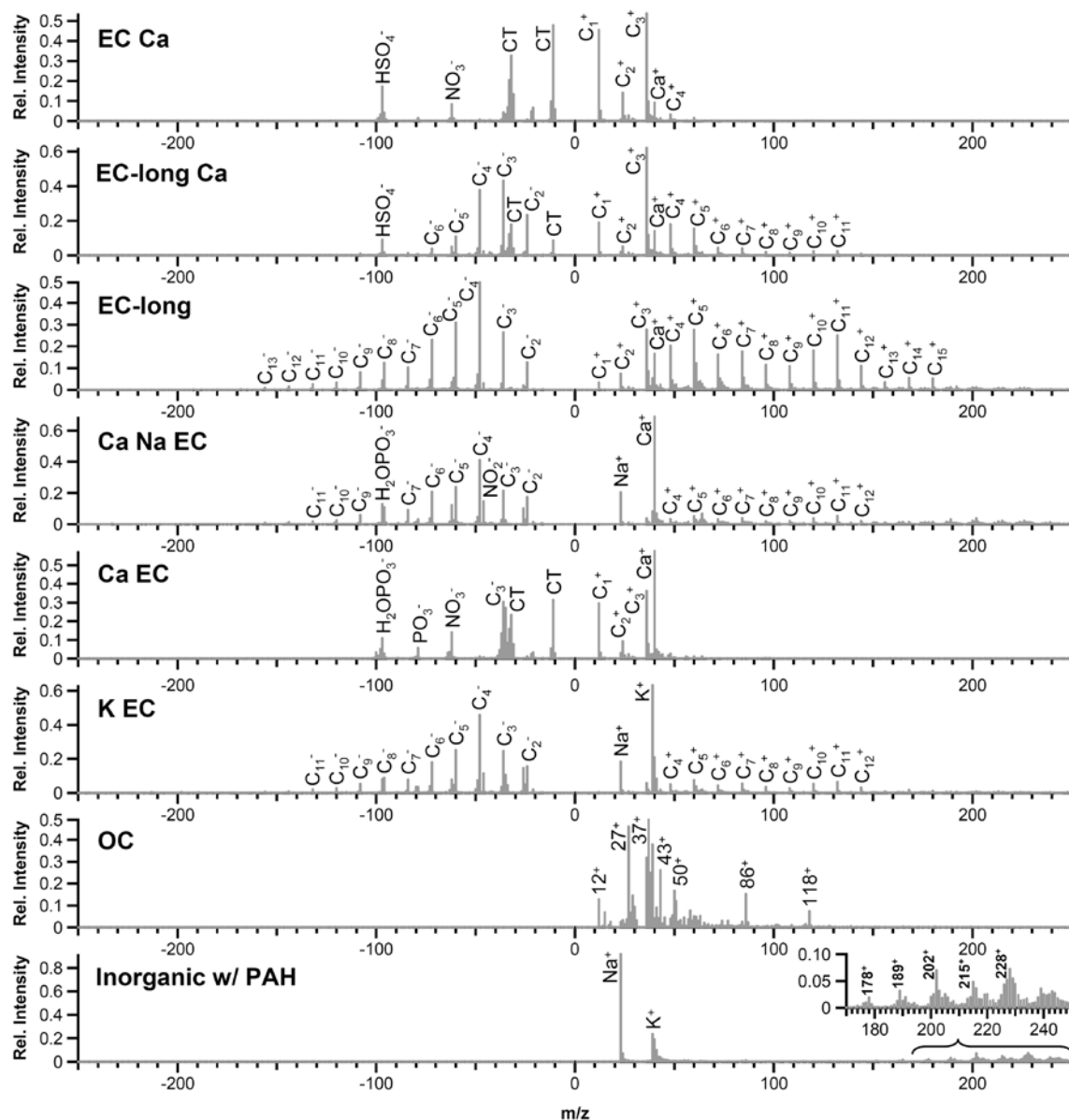


Figure 3 Representative mass spectra for the general chemical classes of ultrafine particles as determined by the UF-ATOFMS. “CT” in the negative spectra represents crosstalk due to the interference of extremely intense peaks in the positive polarity.



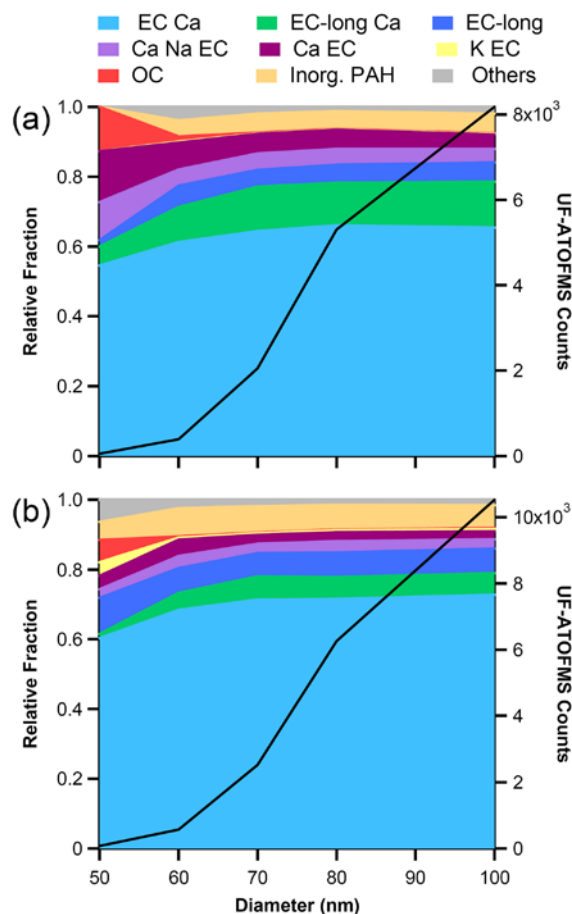


Figure 4 Relative size distribution (10 nm bins) of ultrafine particle types during the summer (a) and fall (b). The black trace represents the total number of ultrafine particles chemically analyzed by the UF-ATOFMS in each 10 nm size bin.

a peak of calcium at  $m/z$  40  $[\text{Ca}]^+$  with the dominating class (EC Ca) representing over 60% of the ultrafine particles. These spectra very closely resemble the variations in the mass spectral signatures detected in previous source characterization studies of vehicle exhaust, showing Ca due to lubricating oil as well as EC (36-38). These particle types vary in their intensities of EC, calcium, sodium (23  $[\text{Na}]^+$ ), phosphate (79  $[\text{PO}_3]^-$  and 97  $[\text{H}_2\text{O}\cdot\text{PO}_3]^-$ ), sulfate (97  $[\text{HSO}_4]^-$ ), and nitrate (46  $[\text{NO}_2]^-$  and 62  $[\text{NO}_3]^-$ ) peaks. The K EC class, marked by intense potassium (39  $[\text{K}]^+$ ) and EC peaks, represents a very small percentage ( $< 1\%$ ) of the ultrafine particles in Riverside. It is not surprising that most of the particles detected by UF-ATOFMS belonged to these EC classes, because EC particles are fractal and thus optically larger. Laboratory tests with the commonly used standard of polystyrene latex spheres (PSLs) have indicated that the UF-ATOFMS does not detect spherical particles with diameters below 90 nm as well. Therefore, this observation indicates that the UF-ATOFMS is very sensitive and uniquely suited to measuring the impact of ultrafine particles from vehicle emissions. The organic carbon (OC) particle type contains hydrocarbon envelopes with peaks at  $m/z$  27  $[\text{C}_2\text{H}_3]^+ / [\text{NCH}]^+$  and 43  $[\text{C}_2\text{H}_3\text{O}]^+ / [\text{CHNO}]^+$ . It also contains peaks at  $m/z$  86 and 118, which are markers for amines (39). The OC type is likely the only spherical particle type detected in the ultrafine mode, and it represents less than 1% of the ultrafine particles detected by the

UF-ATOFMS. The final class shown in **Figure 3** (Inorganic w/ PAH) is dominated by the inorganic species of sodium and potassium but also contains polycyclic aromatic hydrocarbons (PAH) at high  $m/z$ . This class describes ~6% of the ultrafine particles analyzed by the UF-ATOFMS. It is likely that this inorganic ash particle type adsorbs semivolatile PAH as they partition from the gas to particle phase during the cooling of emissions. It is worth noting that a high percentage (~70%) of the particles in the two non-EC containing classes (OC and Inorganic w/ PAH) did not produce appreciable negative ion signals, and thus these two classes are represented in **Figure 3** without negative ion peaks.

**Figure 5** provides the hourly relative fractions for the general chemical classes of the ultrafine particles (50-100 nm) observed by the UF-ATOFMS during the summer (top) and fall (bottom) seasons. The black trace represents the hourly total number of ultrafine particles sized and chemically analyzed by UF-ATOFMS to highlight the periods of higher detection. The missing periods (in white) occur during times when quality control procedures or effective density measurements were being conducted or some other factor led to low particle statistics (< 10 ultrafine particles in that hour). The figure clearly illustrates that the chemical classes associated with vehicle exhaust emissions dominate the ultrafine size mode. Regardless of the time of day, the relative fractions of the ultrafine particle types remain comparatively constant and show no diurnal trend. This agreement is further confirmed by the source apportionment of the SOAR campaigns in Chapter 5 (40). Although vehicle exhaust emissions are a major contributor of primary ultrafine particles and the local vehicle emissions can influence the sampling site at all times, it is expected that the largest contribution will occur during the weekday rush hour periods, which agrees with peaks in the *number* of ultrafine particles detected by the UF-ATOFMS. Despite the lack of large differences in the relative fractions of the chemical classes over time, the number of ultrafine particles detected by the UF-ATOFMS does change significantly. Therefore,

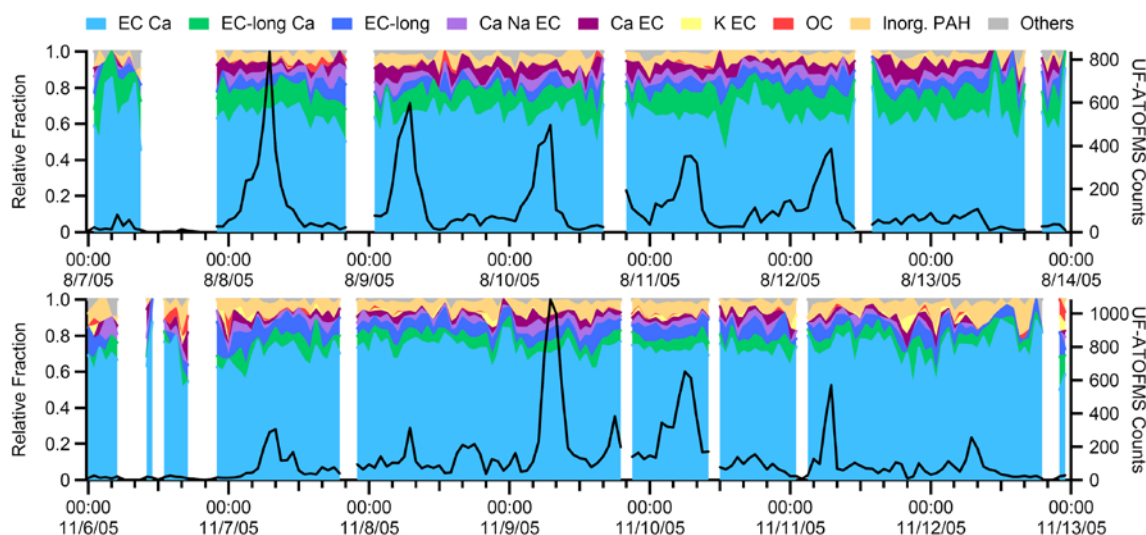
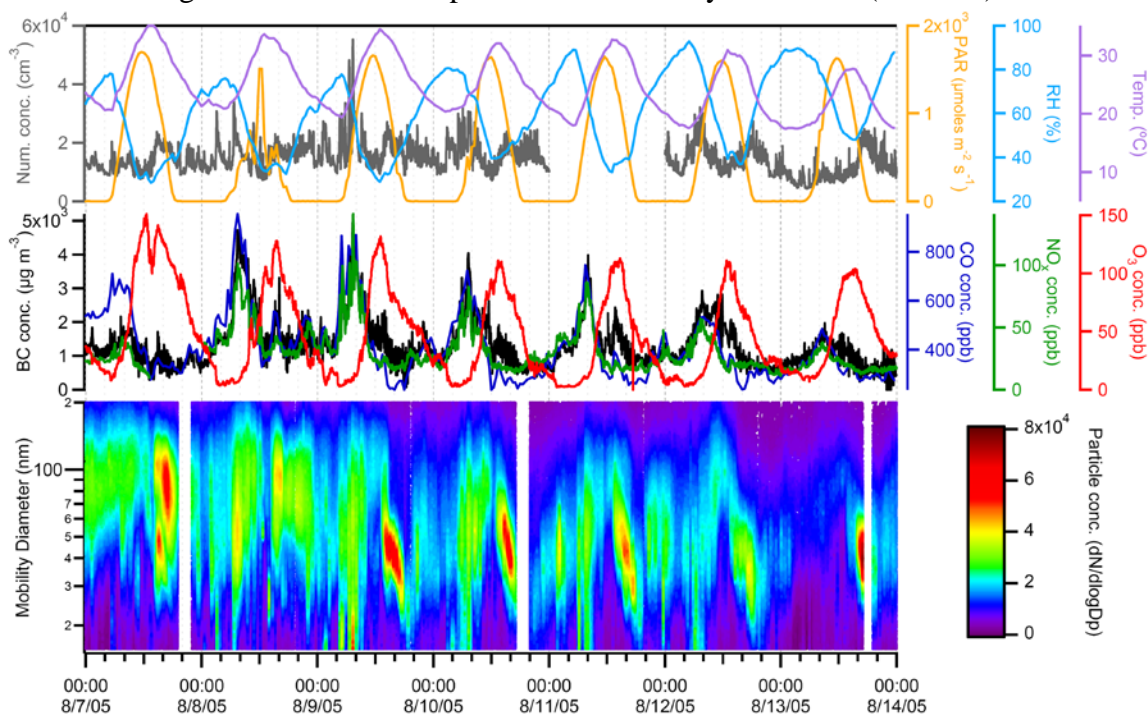


Figure 5 Hourly relative fractions of ultrafine particle types during the summer (top) and fall (bottom). The black trace represents the hourly total of ultrafine particles (50-100 nm) chemically analyzed by the UF-ATOFMS

the UF-ATOFMS unscaled counts represent a good tracer of periods of intense vehicle activity at this location. This observation makes sense, because vehicle exhaust emissions were the only significant source of primary ultrafine particles in close proximity to the sampling site. Any other potential source of ultrafine particles was too far away and the particles would have either coagulated or grown outside of the ultrafine size range before reaching the sampling site. It is also likely that any sources of spherical ultrafine particles would not be detected efficiently by the UF-ATOFMS, as described above.

Multiple gas- and particle-phase instruments, in addition to the UF-ATOFMS, were sampling in Riverside, CA in 2005. These supporting ambient measurements can provide complementary information to the observations made with the UF-ATOFMS. **Figure 6** displays the temporal trends of these other measurements observed for one week (Sunday through Saturday) during the summer. The top panel shows the overall PM<sub>2.5</sub> number concentration (particles cm<sup>-3</sup>) as measured by the UF-CPC, as well as the meteorological parameters (PAR, RH, and temperature). The middle panel presents the black carbon (BC) concentrations determined using the 880 nm wavelength of the aethalometer, in addition to the gas-phase measurements of CO, NO<sub>x</sub>, and O<sub>3</sub>. The bottom contour plot illustrates the particle number concentration detected by the SMPS as a function of electrical mobility diameter (15- 200 nm).

The SMPS measurements showed increased ultrafine particle number concentrations during the weekday morning rush hour period from approximately 5:00 to 10:00 PST, as shown in **Figure 6**. The morning rush hours also were the main time window during which the smallest particles observed by the SMPS (< 30 nm) showed the



**Figure 6:** Temporal trends of gas- and particle-phase measurements, as well as meteorological variables, for one week (Sunday through Saturday) during the summer season.

highest concentrations. In addition, the BC, CO, and NO<sub>x</sub> measurements, which all tracked each other well (lowest R<sup>2</sup> value of 0.71), peaked during this same period (specifically between 8:00 and 9:00 PST). All three measurements correlated with the ultrafine counts from the UF-ATOFMS. For example, the R<sup>2</sup> value between NO<sub>x</sub> concentrations and UF-ATOFMS ultrafine counts was 0.68. Previous studies have reported high correlations between ultrafine number concentrations with both CO and NO/NO<sub>x</sub> measurements at traffic-orientated sampling sites (41-43). Even mass-based BC concentrations have shown significant correlations with ultrafine particle number concentrations (13,20), as also illustrated here. Based on these results, it appears the ultrafine particle number concentration can serve as a good proxy for traffic activity; however, the highest number concentrations (red regions between 30 and 60 nm) measured by the SMPS occurred during the afternoons and not during the traffic-dominated morning rush hour period. Therefore, at least during the summer, the ultrafine particle number concentrations measured by the SMPS are not a unique indicator of traffic activity. The next section explores the SMPS afternoon ultrafine particle peaks in more depth.

### ***b. Afternoon photochemical events***

Previous studies of the diurnal trends of ultrafine particles in the source and receptor sites of the LA Basin have determined that an additional source or sources, other than direct emissions by vehicles, make significant contributions to the number of ultrafine particle in the afternoons of warm months in Riverside. Using the chemical composition data from MOUDI measurements, these studies identified photochemically generated secondary species as the source (44,45). This same photochemical source explains the high concentrations of particles with electrical mobility diameters between 30 and 60 nm in the afternoon hours (13:00–18:00 PST) in **Figure 6**. The daily ultrafine particle event started at the temperature peak which occurs just after the maximum levels of solar radiation and O<sub>3</sub> have been reached on both weekdays and weekends, when traffic activity is reduced. Moreover, the gas-phase tracer concentrations of fresh traffic emissions (CO and NO<sub>x</sub>) were at their minimum values. A detailed study of the aethalometer measurements made during the SOAR campaign also indicated a change in the afternoon mixing state consistent with the condensation of secondary species on account of the diurnal weekday pattern in the absorption cross section, signifying that traffic is not the dominant source of ultrafine particles in the afternoons (46). Additionally, the chemistry of the afternoon particles is expected to be different, because the cloud condensation nuclei (CCN) activity was observed to peak in the afternoon during the summer SOAR campaign (47). As shown in **Figure 2**, few ultrafine (sub-100 nm) particles were chemically analyzed by the UF-ATOFMS during the afternoon photochemical events in the summer. Rather, the UF-ATOFMS detected mostly large (> 100 nm) and aged vehicle particle types and only a few fresh (ultrafine) vehicle particle types during the afternoons. As mentioned, the SMPS measurements indicate that the majority of the ultrafine particles during these events were between 30 and 60 nm, which is below the minimum detection size (50 nm) of the UF-ATOFMS. **Figure 4** shows that the smallest number of ultrafine particles that were chemically analyzed by the UF-ATOFMS was in the 50-60 nm size bin. The fact that the UF-ATOFMS detected few

ultrafine particles during the afternoon serves as further indication that these afternoon particles are not from vehicle exhaust emissions. If the SMPS had been the only instrument sampling at this location, it would have been difficult to rule out the possibility that the high concentrations of ultrafine particles in the afternoon were from vehicles. This study demonstrates how a combination of several different instruments can be used to uniquely identify the source or formation pathway of ultrafine particles.

It is noteworthy that while the SMPS measurements differ based on the time of day, the relative fractions of the particle types detected by the UF-ATOFMS stay relatively constant. Soot-like particles, formed from fossil fuel combustion in vehicles, have irregular shapes and effective densities less than unity. Based on these properties, such particles will have aerodynamic diameters smaller than and electrical mobility diameters larger than their physical diameters (34,48). In other words, the ultrafine particles characterized by the UF-ATOFMS based on their aerodynamic diameters would not be considered ultrafine particles based on their electrical mobility diameters. The effect of this size distinction was observed directly in experiments coupling a DMA with the UF-ATOFMS during the same field campaign; for example, elemental carbon particles with electrical mobility diameters of 400 nm had aerodynamic diameters of 100 nm (48). Under these circumstances, correcting the aerodynamic-based size distribution of the UF-ATOFMS by scaling directly (size for size) to the electrical mobility distribution measured by the SMPS without adjustments for the particle density and shape factor can lead to erroneous results. This discrepancy must always be taken into consideration, especially for the smallest particles ( $\leq 200$  nm) which are the most fractal and have the greatest difference between their aerodynamic and electrical mobility diameters. This information had not been available at the time of analysis for the results presented in Chapter 2. Although the particles detected by the UF-ATOFMS indeed are considered ultrafine particles according to their aerodynamic diameters, the ultrafine particles observed by the SMPS, especially those during the summer afternoon photochemical events, are too small to be optically detected in the UF-ATOFMS. This fact explains why the UF-ATOFMS did not detect a change in the relative number fraction of particle types during the summer afternoon periods.

The lack of the diurnal trend in particles detected by the UF-ATOFMS could arise from the following reasons: only large fractal (non-spherical) vehicle particles with ultrafine aerodynamic diameters are able to optically trigger the timing circuit of the instrument and spherical ultrafine particles from non-vehicular ultrafine particles sources produce particles that are too small to be detected optically with the current configuration. The UF-ATOFMS detection efficiency decreases rapidly with the decreasing diameter of spherical particles; for example, the detection efficiency for the common standard of polystyrene latex spheres (PSLs) is only ~0.3% for 95 nm PSL particles, as opposed to ~44.5% for 290 nm PSL particles (Su et al. 2004). Additional improvements will be needed to directly obtain the chemical information of the ultrafine particles during the afternoon photochemical events by UF-ATOFMS, as they clearly originate from a different source than direct vehicle exhaust emissions and are currently below the UF-ATOFMS detection limit. One possibility is to grow the ultrafine particles by water condensation up to an optically detectable size; however, this condensation process can change the chemistry of the individual particles by gas-to-particle partitioning of water-soluble organic compounds (49-52). Laboratory experiments since

the SOAR campaigns have indicated that placing a neutralizer upstream of the UF-ATOFMS significantly improves the transmission of ultrafine particles to the ionization region of the mass spectrometer. Without the neutralizer, charged particles can deviate from the source region due to the voltages on the source plates of the mass spectrometer with smaller particles deviating more.

Closer examination of the particles analyzed by UF-ATOFMS that were considered to be ultrafine particles based on their size during the summer revealed little difference in the chemistry of the ultrafine particles during the morning rush hour and the afternoon periods. This result suggests that some of the fresh ultrafine vehicle exhaust particles are transported to the site without undergoing significant aging transformations, which would cause their growth into larger sizes. On the other hand, larger particles (>100 nm), which are not shown here, do illustrate chemical differences between the mornings and afternoons (31). Many of these larger afternoon particles are morning ultrafine particles that have grown and transformed by aging processes, becoming CCN active (40,47). Once spherical ultrafine particles from non-vehicle sources have aged and grown into larger sizes, they can then be optically detected with the UF-ATOFMS.

The afternoon photochemical events in Riverside have different properties from the different types of nanoparticle and ultrafine particle events observed elsewhere, because they show a reduction in particle size rather than growth behavior (21). The loss of chemical species from the particles via evaporation is most likely not the cause of the reduction in particle size during the afternoon events in Riverside, because the temperature is cooling down and the RH is increasing at the start of the event. Moore et al. reported similar behavior with their summer 2006 campaign near downtown LA; however, their photochemical event begins immediately following the morning commute and before the peak in O<sub>3</sub> (53). In Riverside, there are at least a few hours between the end of the morning traffic periods and the beginning of the afternoon photochemical events. Because Riverside is downwind of the LA Basin, this time difference suggests that, unlike in downtown LA, the necessary precursors responsible for the afternoon photochemical events are not immediately available in Riverside and must be transported to the site. Therefore, these results suggest that different sources and processes control the formation and most likely the chemistry of ultrafine particles throughout the day in Riverside; primary sources are dominant during the morning hours, and secondary sources control the afternoon hours.

### *c. Seasonal differences*

The temporal trends of the gas- and particle-phase measurements for one week (Sunday through Saturday) during the fall season are shown in **Figure 7**. As described in Qin et al., the summer weekdays in Riverside exhibited consistent diurnal trends, whereas PM<sub>2.5</sub> during the fall season was better characterized as being episodic; the week shown features a high mass period (November 6 15:00 – November 7 18:00) of stagnant meteorological conditions and a PM<sub>2.5</sub> mass concentration of 106  $\mu\text{m}^{-3}$ , as well as a scavenging period (November 8 22:00 – November 11 13:00) with light precipitation events and low mass concentrations (31). Likewise, the fall trends of ultrafine particle number concentrations show less diurnal trends than in



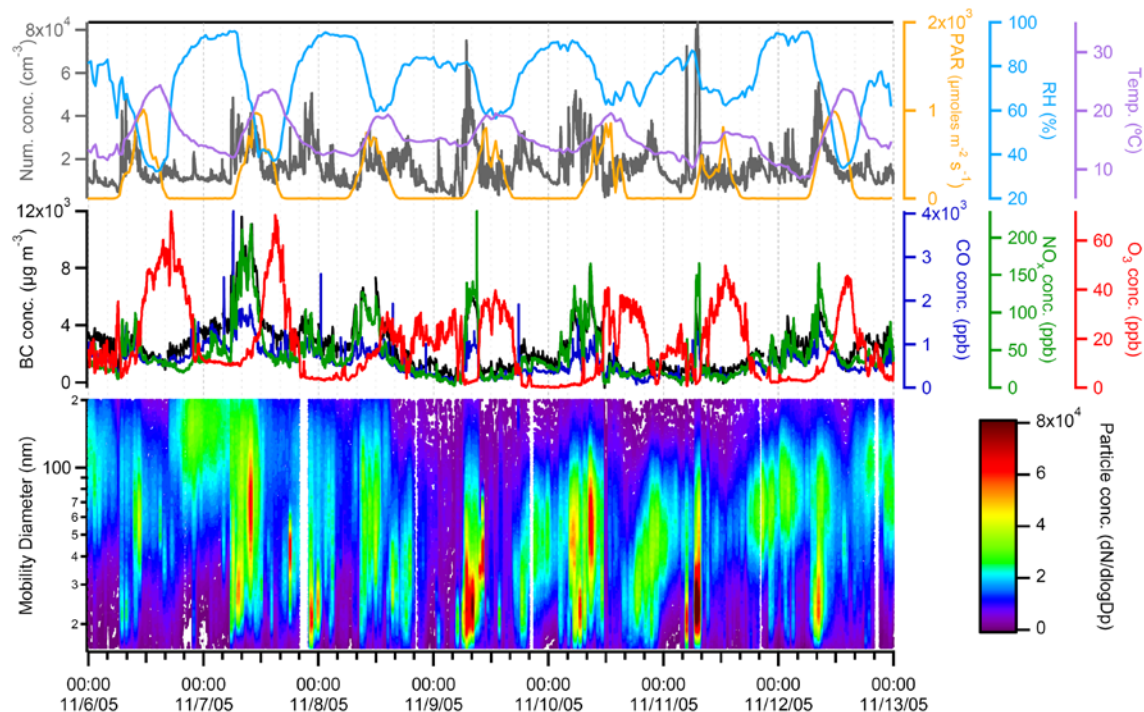


**Figure 7: Temporal trends of gas- and particle-phase measurements, as well as meteorological variables, for one week (Sunday through Saturday) during the fall season.**

the summer with the exception of the morning rush hour period, as shown in **Figure 7**. During the high mass period (November 6 15:00 – November 7 18:00), few ultrafine particles existed, most likely due to the presence of high numbers of larger particles (and therefore large surface areas available) with which the ultrafine particles could quickly coagulate. The precipitation events during the scavenging period reduced the concentrations of particles in all size ranges; however, after the rain ended, the ultrafine particles from local sources were the first to appear again at high concentrations. The highest number concentrations (based on the UF-CPC and SMPS measurements) correlated with the peaks in BC, CO, and NO<sub>x</sub> concentrations, agreeing with previous reports that vehicular emissions are the major contributor to particle number concentrations during the fall season in Riverside (23). The photochemical activity (and therefore afternoon photochemical ultrafine events) is seasonal (54), as the November PAR values are nearly 50% of those during August. Consistent with this lower PAR, very low afternoon ultrafine particle number concentration peaks were detected. The lack of afternoon ultrafine events during the fall season helps explain why the average ultrafine (15-100 nm) number concentration based on SMPS measurements during the fall ( $6.7 \times 10^5$  particles cm<sup>-3</sup>) was ~70,000 particles cm<sup>-3</sup> lower than that during the summer ( $7.4 \times 10^5$  particles cm<sup>-3</sup>).

Although the fall UF-ATOFMS raw ultrafine counts (shown at the bottom of **Figure 5**) tend to track the UF-CPC, BC, NO<sub>x</sub>, and CO measurements, the morning rush hour spikes are not exactly consistent with those during the summer season. The Monday and Tuesday morning peaks during the fall are not as intense as the morning increases observed during the summer. The nearest major freeway was located ~600 m to the west of the sampling site. The local winds during the summer season came from a westerly

direction nearly all of the time, whereas the fall winds were split between the westerly (daylight hours) and easterly (nighttime hours) directions (31). In addition, the summer wind speeds were much stronger than the fall wind speeds, carrying the freshly emitted vehicle exhaust particles more rapidly to the sampling site. Therefore, both the meteorological conditions and episodic behavior resulted in less ultrafine vehicle particles being detected by the UF-ATOFMS during the fall.

#### ***d. Comparison of ultrafine particle measurements***

Because each of the ultrafine instruments used in this study make measurements based on different particle properties, it is interesting to compare their results. Differences in ultrafine particle detection between the SMPS and UF-ATOFMS were already discussed above. As shown in **Figure 6**, there is discrepancy between the summer SMPS measurements and the overall particle number concentrations determined by the UF-CPC. The UF-CPC shows increased concentrations during the morning rush hour periods (and likewise during the fall as seen in **Figure 7**), but it responds little to the afternoon photochemical ultrafine events, which displayed the highest concentrations observed by the SMPS during the summer. Because the fall season did not have significant afternoon photochemical events, the instruments agreed well with each other during the fall (**Figure 7**). Previous studies have shown significant differences in SMPS and CPC performance when there are high number counts for small sized particles (55,56). However, the numbers provided by the UF-CPC in the current study do not exceed its upper limit of  $10^5$  particles  $\text{cm}^{-3}$  nor are the particles (30-60 nm) of this event pushing the lower detection limit of the instrument (3 nm) (27).

This disagreement was not unique to this specific instrument, because its measurements compared well to those of other CPCs at the same location, including ones that use an alternative vapor (water) for particle growth (57). All CPC instruments followed the same temporal trend despite the use of different condensable vapors, and none appeared to detect the ultrafine particles during the photochemical events. Particles made of pure organic materials can be detected at 30 nm, so it is unlikely that the minimum detection cut point is higher than the diameters of these particles (58). It is possible to grow these particles through condensation, as they were optically counted by the CPC in the SMPS system. However, the particles introduced to the CPC after passing through the DMA were generally of uniform size, and there was a lower overall concentration of particles at a given time compared to the other CPCs. It may be possible that when all particles of a broad size range are sampled at the same time by the CPC, particles composed mainly of secondary materials recondense on larger sized particles rather than grow themselves. In addition, a laboratory comparison of a SMPS and CPC using monodisperse NaCl aerosols determined that more efficient neutralization of the charged particles upstream of the instruments improves their agreement, because the neutralizer that is part of the SMPS system left more multiply charged particles than predicted, which falsely gave the SMPS higher measurements (55). It is not yet known if this approach will work for the secondary aerosols produced in photochemical events. Most likely, the disagreement is caused by a combination of over-counting in the SMPS measurements due to inefficient neutralization and under-counting in the UF-CPC measurements due to high particle number concentrations, though it is important that future studies address this discrepancy occurring during the summer afternoon periods.



In summary, the UF-ATOFMS measurements provided single particle chemical information on the ultrafine particles based on their aerodynamic diameters. The major ultrafine particle types observed in Riverside resembled the mass spectral signatures observed in lubricant oil combustion from vehicular exhaust emissions. With this information on the chemical classes in combination with the measurements by supporting gas- and particle-phase instruments, it was determined that vehicle exhaust emissions are the major local source contributing to primary ultrafine particles during weekday morning rush hour periods. During the summer season only, an additional source of secondary ultrafine particles was detected during afternoon photochemical events that occurred after LA pollutants were transported to the site.

Real-time measurements of particle size and chemistry coupled with gas-phase measurements have provided unique insight into the daily and seasonal variations of ultrafine particles. In this study, it is demonstrated how ultrafine particle sources (and hence chemistry) can rapidly change over the course of the day, as well as show a strong seasonal dependence. High ultrafine particle concentrations were observed during different periods and seasons, yet the chemistry of the particles was often different. Thus, future studies of health effects aimed at understanding the impacts of ultrafine particles must take into account their sources, degree of aging, and overall chemistry rather than solely relying on their number concentration as a proxy.

#### **iv. Acknowledgements**

The authors express their gratitude to the entire Prather group for their help in the preparation and overall support of these studies. We thank Megan McKay and the Goldstein research group at the University of California, Berkeley for the summer CO measurements and the meteorology data. We also acknowledge Professor Paul Ziemann (University of California, Riverside) for hosting the SOAR field campaigns, as well as Professor Jose Jimenez (Colorado University, Boulder) and Dr. Ken Docherty (Colorado University, Boulder) for setting up the logistics. Finally, we thank Dr. Susanne Hering (Aerosol Dynamics) for the use of her CPC data and helpful suggestions. Funding for this project was supplied by the California Air Resources Board (Contract 04-336).

## **2. Characterization of the Single Particle Mixing State of Individual Ship Plume Events measured at the Port of Los Angeles**

### **i. Introduction**

Ship emissions are among the least regulated forms of anthropogenic pollution given the challenges involved in establishing international policies. Ship emissions impact climate by initiating cloud formation and altering earth's radiation budget (59,60). Ships emit high concentrations of soot and heavy metals (i.e. vanadium and nickel) (61,62), in addition to an estimated 2.4 tons of SO<sub>2</sub> globally, producing up to 10% of sulfate mass globally through atmospheric reactions (63). Over the next century, SO<sub>2</sub> levels are predicted to rise significantly as global commerce expands (63). Ship emissions have been shown to have negative effects on human health through exposure studies and epidemiological models (64-66). For example, inhaled vanadium particles are toxic and synergistic effects with nickel and sulfate have been shown to enhance toxicity (65). To determine effective strategies for reducing the impact of shipping on climate and health, recent studies have focused on improving ship emission inventories which are used to estimate future scenarios for gas phase concentrations (67). Efforts to regulate shipping emissions have been difficult due to fuel and upgrade costs and international dependence on foreign trade (68,69).

Particulate emissions from ships have been characterized by multiple analytical methods including energy dispersive x-ray fluorescence measurements of particulate matter on filters (62), ion chromatography (IC) of particulate matter extracted from filters (61), real-time mass-based measurements (70,71), particle counters (72), cloud condensation nuclei measurements (70), and size distribution measurements (62). These measurements have led to updated emission inventories and emission factors for aerosol mass and particle number for ship emissions (70,71). Real-time, single-particle mass spectrometry has also been used to identify ship emissions at locations away from the source regions (73,74). Herein, we report in-situ measurements of the chemical mixing state of particles in fresh ship plumes measured at the Port of Los Angeles.

### **ii. Experimental**

#### ***a. Sampling Information***

Ambient air sampling was conducted from November 16–26, 2007 at the Port of Los Angeles (LA) on Terminal Island in San Pedro, California. Particles were sampled through a four meter sampling mast, seven meters above the ground at a sampling site 500 meters east of the center of the main channel. Wind direction and speed were measured using a R.M. Young wind monitor. Winds exhibited a consistent diurnal pattern with southerly sea breezes during the day and light nocturnal land breezes from the north. Radio transmissions of the location, speed, and heading of ships entering and exiting the port were recorded in real-time with an automated identification system (AIS) antenna in La Jolla, CA (75). These transmission signals are required to be sent every minute for ships at sea over 299 gross tons by the International Maritime Organization.

### ***b. Gas and Particle Peripheral Instrumentation***

Gas phase measurements were made of NO<sub>x</sub> (Thermo Environmental Instruments (TEI) Model 42C), O<sub>3</sub> (TEI Model 49), and SO<sub>2</sub> (TEI Model 43). Particle size distributions were measured with a scanning mobility particle sizer (SMPS, TSI Model 3936L) operating from 10 – 600 nm at a time resolution of 5 minutes; black carbon (BC) concentrations (ng/m<sup>3</sup>) were measured using an aethalometer (Magee Scientific AE31).

### ***c. Aerosol Time-of-Flight Mass Spectrometry (ATOFMS)***

The design and details of the ultrafine (UF)-ATOFMS used in this study are described in detail elsewhere (2). This instrument measures the size and chemical composition of individual particles between 100-1000 nm during this study. Briefly, particles are introduced into the UF-ATOFMS through an aerodynamic lens into a differentially pumped vacuum chamber where the particles are accelerated to a size-dependent velocity. Particles pass through two 532 nm continuous wave lasers located 6 cm apart. Particle speed is used to determine vacuum aerodynamic diameter by calibration with polystyrene latex spheres of known size. Sized particles are individually desorbed and ionized in the mass spectrometer source region by a 266 nm Q-switched Nd:YAG laser (1.2-1.4 mJ). Positive and negative ions produced from individual particles are detected using a dual-reflectron time-of-flight mass spectrometer.

### ***d. Single Particle Analysis***

During sampling at the Port of LA, the aerodynamic size and chemical composition of 1,245,041 particles were analyzed using an UF-ATOFMS. Size and mass spectral information were imported into MatLab 6.5.1 (The Mathworks Inc.) and analyzed utilizing YAADA 1.2 ([www.yaada.org](http://www.yaada.org)). Individual particles were analyzed via two methods: 1) mass spectral ion intensities, aerodynamic size, and temporal information and 2) clustering via an adaptive resonance theory based neural network algorithm (ART-2a) at a vigilance factor of 0.8 (35). ART-2a classifies individual particles into separate clusters based on the presence and intensity of ion peaks in individual single-particle mass spectra. Peak identifications within this paper correspond to the most probable ions for a given mass/charge (*m/z*) ratio. General particle types are defined by the characteristic chemical species in an attempt to simplify the naming scheme; these labels do not reflect all of the species present within a specific particle class.

## **iii. Results and Discussion**

### ***a. Ship Identification***

Characteristics of each positively identified ship plume over a 10 day period are listed in **Table 3** which includes: the peak time of the observed plume, length of time the plume was observed, calculated transport time from the point of emission to the peak of the plume at the sampling location using wind speed, peak particle number concentration, characteristic particle type, number of particles chemically characterized by the UF-ATOFMS, number fractions of OC-V-sulfate and fresh soot particles present during the plume detection period. The times when different ships passed the sampling location

were determined through a combination of arrival and departure logs (76), AIS ship position recordings, and pictorial documentation. As an example, **Figure 8** shows the arrival of the vessel Container1b on November 19, 2007 at 03:30 (PST). Red markers (1 minute resolution) represent the ship's position as recorded by the AIS, and the green diamond represents the sampling location. The blue line shows the path of the plume (550 meters) to the sampling location based on measured wind direction ( $292^{\circ}$ ) and speed (0.6 m/s). Ships that could be positively identified by time, position, and wind speed/direction are analyzed in detail; however, numerous ships and plumes passed the site during the sampling period that could not be confidently assigned using the criteria listed above. Due to changing wind direction and wind speed, calculated plume travel times to the sampling location varied from 5-20 minutes.

| Ship<br>Plume | Plume Peak<br>Time (PST) | Duration<br>(min) | Age<br>(min) | Peak Num Conc<br>(#/cm <sup>3</sup> ) | Identifying<br>ATOFMS Type | ATOFMS<br>Particles | Number Fract<br>OC-V-Sulfate | Number Fract<br>Fresh Soot |
|---------------|--------------------------|-------------------|--------------|---------------------------------------|----------------------------|---------------------|------------------------------|----------------------------|
| Container1a   | 11/17 5:00               | 15                | 15           | 9217                                  | Fresh Soot                 | 517                 | 0.6                          | 30.0                       |
| Container2    | 11/17 6:05               | 20                | 15           | 8757                                  | OC-V-Sulfate               | 752                 | 18.8                         | 3.2                        |
| Container3    | 11/18 15:25              | 10                | 10           | 9884                                  | OC-V-Sulfate               | 324                 | 9.9                          | 1.9                        |
| Container1b   | 11/19 3:30               | 10                | 15           | 11310                                 | OC-V-Sulfate               | 1056                | 17.0                         | 2.1                        |
| Tanker1a      | 11/19 18:05              | 20                | 20           | 44697                                 | OC-V-Sulfate               | 747                 | 24.0                         | 4.8                        |
| Container4    | 11/20 17:20              | 25                | 10           | 21177                                 | OC-V-Sulfate               | 734                 | 26.3                         | 2.6                        |
| Tanker1b      | 11/20 18:20              | 15                | 10           | 12792                                 | Both                       | 345                 | 34.2                         | 9.3                        |
| Container5    | 11/20 19:15              | 10                | 10           | 11806                                 | Fresh Soot                 | 1220                | 1.5                          | 25.3                       |
| Tanker2       | 11/21 5:35               | 25                | 45           | 8927                                  | Both                       | 756                 | 6.5                          | 7.3                        |
| Container6    | 11/24 12:25              | 10                | 10           | 12984                                 | Both                       | 2077                | 10.8                         | 25.6                       |
| CruiseShip1   | 11/24 16:25              | 15                | 5            | 30231                                 | Fresh Soot                 | 2733                | 3.6                          | 12.6                       |
| Container7    | 11/25 18:10              | 20                | 30           | 9593                                  | Fresh Soot                 | 1370                | 3.6                          | 9.5                        |

**Table 3: Characteristics of ship plumes sampled including: Ship plume, plume peak time, plume duration, plume age, peak number concentration, identifying ATOFMS particle type, number of ATOFMS particles, number fraction of OC-V-sulfate particles, and number fraction of fresh soot particles.**

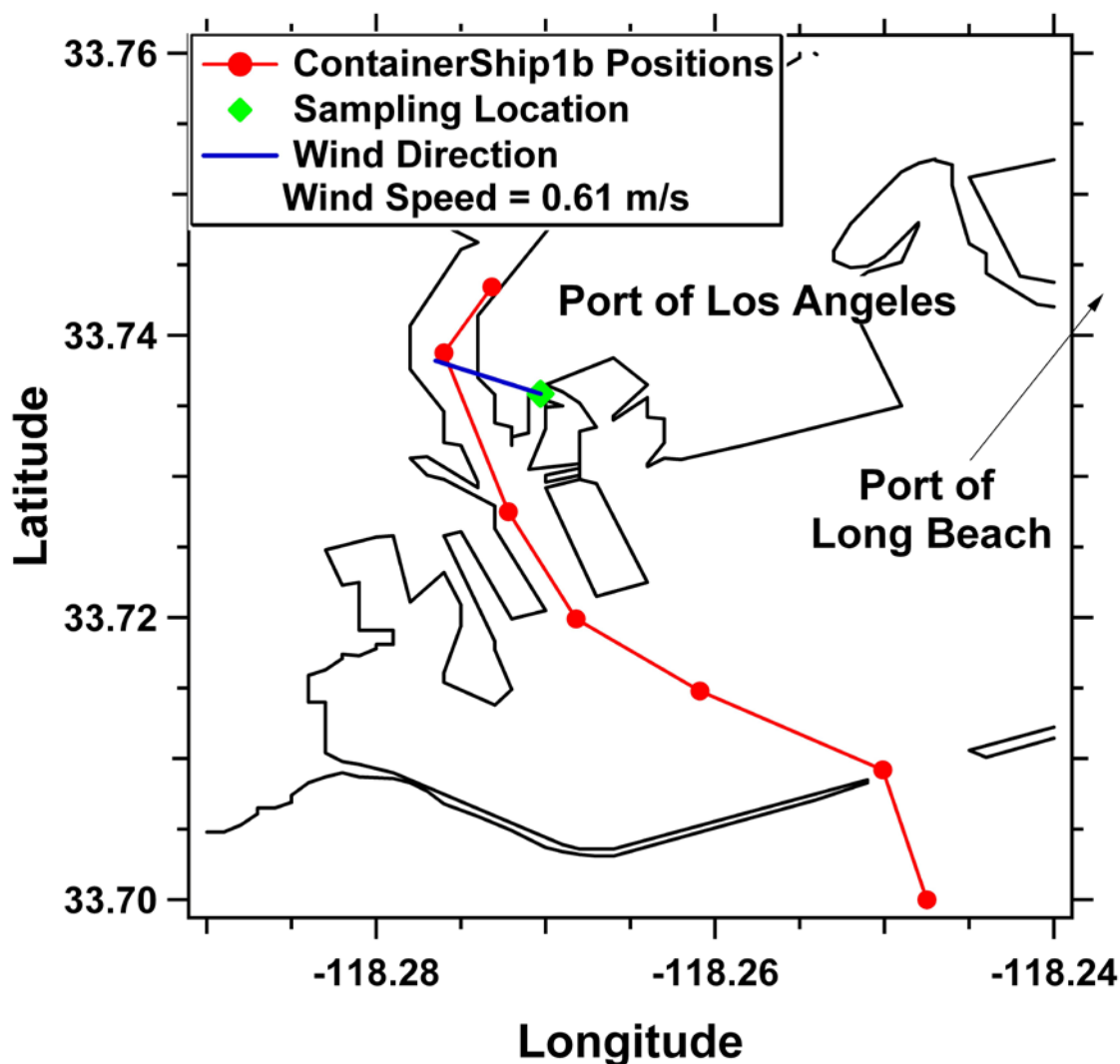


**Figure 8:** Map showing the Port of LA. The green diamond represents the sampling location and the red markers and line represent the one minute resolution positions and course of a container ship as it departed from the Port of LA at 03:30 on November 19, 2007. The blue line represents the average wind direction during transport of the plume to the sampling location.

### ***b. Plume Characterization***

Characteristics of a representative plume observed on November 19, 2007 at 03:30 from the vessel Container1b are shown in **Figure 9**. The top portion shows  $\text{SO}_2$ ,  $\text{NO}_x$ , and BC concentrations increasing sharply from background conditions at the onset of the plume and  $\text{O}_3$  decreasing due to reaction with NO (62,72). Gas phase data were used to qualitatively identify the presence of ship plumes. The duration of this plume at the sampling site was ~15 minutes, which is similar to previously observed timescales (62) (13.6 min.). Similar trends for gas phase species were observed in most plumes; Table 4 lists  $\text{SO}_2$  and  $\text{NO}_x$  concentrations during different plume events and provides a detailed discussion. The bottom portion of **Figure 9** shows the temporal evolution of the

size-resolved particle number concentrations with 5 minute resolution during the plume sampling period. A rapid increase in the total number concentrations of 10-600 nm particles (white line) occurred as the plume passed the sampling location, representing an increase over background levels from 5000/cm<sup>3</sup> to 11,000/cm<sup>3</sup>. The mode and shape of the size distribution did not shift significantly while sampling this plume.

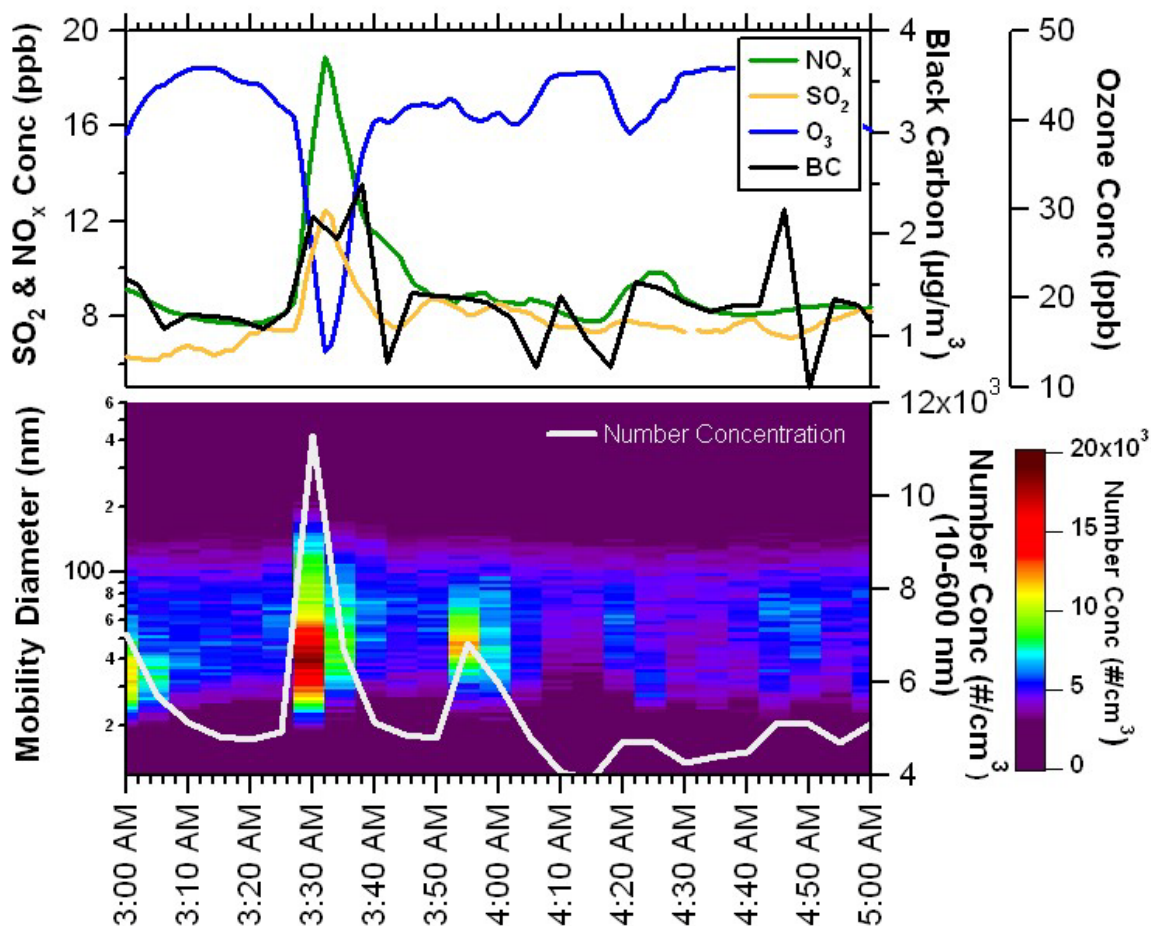


**Figure 9:** Identification of the plume of Container1b. Gas phase measurements included SO<sub>2</sub> (orange), NO<sub>x</sub> (green), and O<sub>3</sub> (blue). Particle phase measurements were of black carbon (black), particle number concentration (white), and size-resolved number concentrations over time (color matrix).

### *c. In Plume Gas Phase Chemistry and Concentrations*

The expected loss of O<sub>3</sub> shown in **Figure 9** should have a 1:1 ratio to the gain in NO<sub>x</sub> (assuming NO<sub>x</sub> is primarily NO in a fresh plume), but this was not observed. A number of factors may have contributed to this including: additional species reacting with NO and O<sub>3</sub> and the presence of aqueous particles and droplets that could have scavenged gas phase species. The peak concentration in SO<sub>2</sub>, NO<sub>x</sub>, and O<sub>3</sub> during the different ship plumes is given in Table 4, along with background concentrations and the net concentration increase. The ratio of NO<sub>x</sub>/SO<sub>2</sub> is also given which can be an indicator of fuel type. Residual fuels have higher concentrations of sulfur and thus produce higher

concentrations of SO<sub>2</sub>, while distillate fuels have less sulfur and produce less SO<sub>2</sub> (77). Changes in the gas phase data to lower NO<sub>x</sub>/SO<sub>2</sub> (ppbv/ppbv) ratios presented here correspond to changes in particle chemistry in the plumes with higher levels of OC-V-sulfate particle levels. In contrast, fresh soot plumes have higher NO<sub>x</sub>/SO<sub>2</sub> ratios.

|             | SO <sub>2</sub> (ppbv) |          |             | NO <sub>x</sub> (ppbv) |          |              | O <sub>3</sub> (ppbv) |          |             | NO <sub>x</sub> /SO <sub>2</sub> |
|-------------|------------------------|----------|-------------|------------------------|----------|--------------|-----------------------|----------|-------------|----------------------------------|
|             | Max                    | Baseline | Peak        | Max                    | Baseline | Peak         | Min                   | Baseline | Peak        | Ratio                            |
| Container1a | 7.2                    | 3.5      | <b>3.7</b>  | 26.2                   | 7.3      | <b>18.9</b>  | 30.0                  | 55.1     | <b>25.1</b> | <b>5.1</b>                       |
| Container2  | 7.7                    | 3.4      | <b>4.3</b>  | 16.7                   | 7.9      | <b>8.8</b>   | 19.7                  | 54.9     | <b>35.2</b> | <b>2.0</b>                       |
| Container3  | 11.2                   | 5.0      | <b>6.2</b>  | 19.1                   | 10.7     | <b>8.4</b>   | 45.0                  | 68.0     | <b>23.0</b> | <b>1.4</b>                       |
| Container1b | 12.5                   | 7.4      | <b>5.1</b>  | 18.9                   | 7.7      | <b>11.2</b>  | 14.0                  | 45.8     | <b>31.8</b> | <b>2.2</b>                       |
| Tanker1a*   | 47.7                   | 18.5     | <b>29.2</b> | 160.0                  | 58.0     | <b>102.0</b> | No Min                | No Min   | <b>N/A</b>  | <b>3.5</b>                       |
| Container4  | 10.7                   | 4.1      | <b>6.6</b>  | 39.5                   | 14.9     | <b>24.6</b>  | 27.8                  | 57.1     | <b>29.3</b> | <b>3.7</b>                       |
| Tanker1b    | 6.3                    | 3.2      | <b>3.1</b>  | No Peak                | No Peak  | <b>N/A</b>   | No Min                | No Min   | <b>N/A</b>  | <b>N/A</b>                       |
| Container5  | 4.1                    | 3.1      | <b>1.0</b>  | 38.0                   | 7.1      | <b>30.9</b>  | 37.4                  | 45.4     | <b>8.0</b>  | <b>30.9</b>                      |
| Tanker2     | 12.0                   | 6.7      | <b>5.3</b>  | 32.4                   | 10.1     | <b>22.3</b>  | 8.7                   | 38.6     | <b>29.9</b> | <b>4.2</b>                       |
| Container6  | 12.0                   | 8.6      | <b>3.4</b>  | 41.6                   | 15.8     | <b>25.8</b>  | 23.7                  | 44.8     | <b>21.1</b> | <b>7.6</b>                       |
| CruiseShip1 | 10.8                   | 6.6      | <b>4.2</b>  | 52.3                   | 11.7     | <b>40.6</b>  | 26.0                  | 46.4     | <b>20.4</b> | <b>9.7</b>                       |
| Container7  | 9.0                    | 4.7      | <b>4.3</b>  | 13.2                   | 10.5     | <b>2.7</b>   | 23.0                  | 35.1     | <b>12.1</b> | <b>0.6</b>                       |

\* night-time chemistry altered by land breeze in Long Beach leading to high NO<sub>x</sub> & SO<sub>2</sub> levels, but low O<sub>3</sub>

Table 4: Gas phase concentrations (max, baseline, and peak) of SO<sub>2</sub>, NO<sub>x</sub>, and Ozone during different plume events are shown along with the NO<sub>x</sub>/SO<sub>2</sub> ratio.

#### *d. Unique Plume Chemistry*

Two types of ship plumes were observed in this study: one with a large number fraction of internally mixed organic carbon, vanadium, and sulfate (OC-V-sulfate) particles and a second with a large number fraction of freshly emitted soot particles. The average mass spectrum of the OC-V-sulfate particle type is shown in **Figure 10**, showing intense vanadium peaks at <sup>51</sup>V<sup>+</sup> and <sup>67</sup>VO<sup>+</sup> and organic carbon markers including <sup>27</sup>C<sub>2</sub>H<sub>3</sub><sup>+</sup>, <sup>29</sup>C<sub>2</sub>H<sub>5</sub><sup>+</sup>, <sup>37</sup>C<sub>3</sub>H<sup>+</sup>, and <sup>43</sup>C<sub>2</sub>H<sub>3</sub>O<sup>+</sup>, as well as a strong bisulfate ion signal (<sup>97</sup>HSO<sub>4</sub><sup>-</sup>). A sulfuric acid cluster peak (<sup>195</sup>H<sub>2</sub>SO<sub>4</sub>•HSO<sub>4</sub><sup>-</sup>) was observed for ~80% of these OC-V-sulfate particles. Residual fuels used in shipping contain much higher concentrations of heavy metals than distillate fuels (77) with previous ATOFMS source studies of cars and trucks showing <1% of particles mixed with vanadium (36). Further, previous studies have noted the correlation of vanadium and sulfur in ambient single particles and attributed these particles to fuel oil combustion (78).

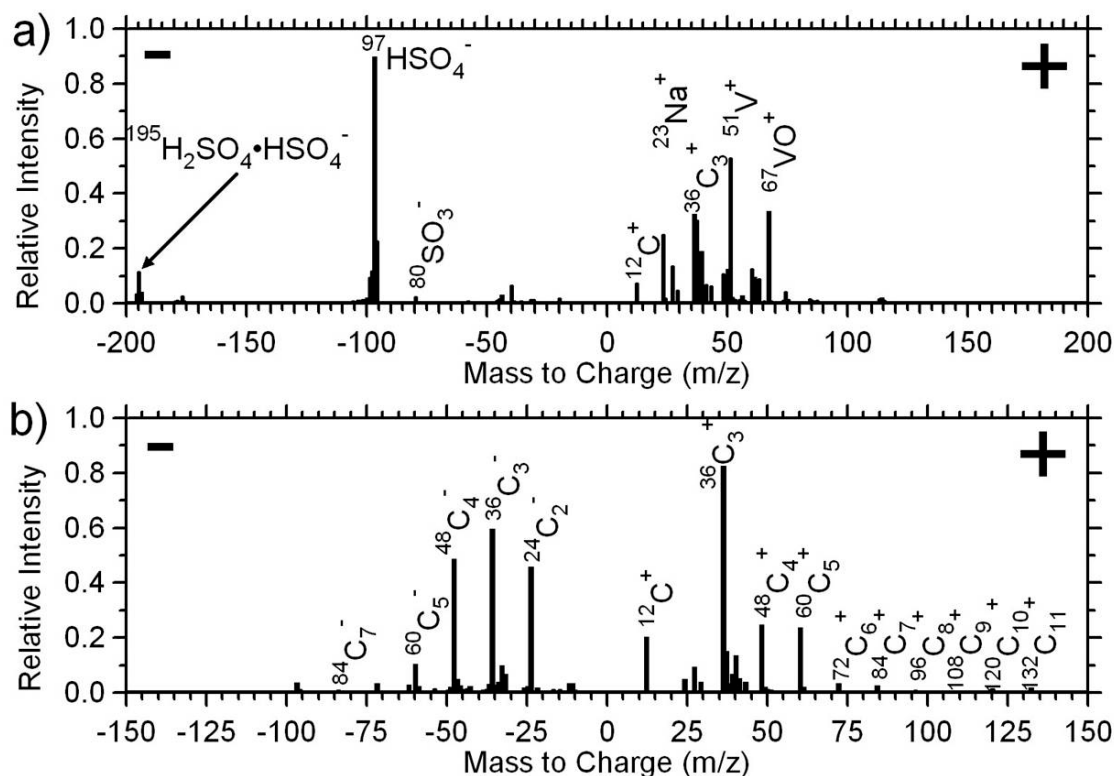


**Figure 10:** Average negative and positive ion mass spectra for the OC-V-sulfate (a) and fresh soot (b) particle types.

The average mass spectrum of the soot (or elemental carbon) particle type is shown in **Figure 10**, characterized by both positive and negative carbon cluster ions (e.g.,  $^{12}\text{C}_1^+$ ,  $^{24}\text{C}_2^+$ , ...,  $\text{C}_n^+$ ). These freshly emitted soot particles did not contain significant sulfate or nitrate ion markers, likely due to limited time for atmospheric aging between the point of emission and sampling. This contrasts most background particle types observed at the Port of LA which contained significant amounts of nitrate and/or sulfate, including other elemental carbon particle types, as discussed below. Particle types similar to these fresh soot particles have been observed during source testing of both cars burning gasoline and trucks burning distillate (i.e. diesel) fuel (36,37). Detailed information on mass spectral variability within the OC-V-sulfate and fresh soot types is included in the Supplemental Information. While other particle types were present within these plumes, the OC-V-sulfate and fresh soot particle types were observed as characteristic source markers for the two different plume types. Plumes were labeled as OC-V-sulfate and/or fresh soot when each particle type represented greater than 5% of particles sampled during the plume.

For the residual fuel combustion ship plumes described herein, the OC-V-sulfate type represented 10-34% of particles sampled in the 100-500 nm size range. The distinct OC-V-sulfate and fresh soot plumes likely result from the combustion of different fuels, with residual fuel oil producing the OC-V-sulfate plumes and distillate fuel forming the fresh soot plumes. The soot plumes also had elevated levels of Ca-ECOC particles. The presence of Ca-ECOC particles agrees with filter measurements in a marine distillate



exhaust study, which found calcium to be ~25% of the relative weighted emission factor for trace elements compared to <5% in residual fuel combustion exhaust (79). The Ca-ECOC particle type has been linked to distillate (i.e. diesel) fuel in previous ATOFMS source characterization studies (37); the mass spectrum is included in the Supplemental Information. While the average ratio of NO<sub>x</sub> to SO<sub>2</sub> (ppbv/ppbv) during the study was 3.7, it was lower in the OC-V-sulfate plumes (average 2.6, range: 1.4-4.2) and higher in the soot plumes (average 11.6, range: 0.6-30.9). This suggests a relative enrichment of SO<sub>2</sub> in the V-plumes as would be expected when burning residual fuels with high sulfur content (max 3.5 % (m/m)) (77). A study comparing an auxiliary engine burning distillate fuel and a main engine burning residual fuel found significantly higher vanadium levels associated with the residual fuel combustion and higher levels of calcium with the distillate fuel combustion, which agrees with diesel source testing by the UF-ATOFMS (37,79). This is also consistent with our findings of OC-V-sulfate particles in the residual fuel combustion plume and Ca-ECOC particles in the distillate fuel combustion plume. In addition, the amount of sulfate from IC of particulate matter in filter extracts does not shift significantly with ship engine load for residual or distillate fuels, suggesting that the presence of OC-V-sulfate particles under normal operating conditions further indicates a residual fuel combustion plume and a lack of OC-V-sulfate indicates a distillate fuel combustion plume (61).

#### *e. Details on the OC-V-sulfate and Fresh Soot Particle Types*

The digital color stack (DCS) for the OC-V-sulfate particle type is shown in **Figure 11**. The x-axis is mass-to-charge and the y-axis shows the fraction of particles within this type containing a specific peak. The color represents the fraction of particles with different peak areas; a peak area > 500 (arbitrary units) was used to exclude noise in the spectra. The ion peaks with the largest fraction and highest intensity in the positive spectrum are the mass to charges corresponding to vanadium (<sup>51</sup>V<sup>+</sup> and <sup>67</sup>VO<sup>+</sup>) and organic carbon (<sup>27</sup>C<sub>2</sub>H<sub>3</sub><sup>+</sup>, <sup>36</sup>C<sub>3</sub><sup>+</sup>, <sup>37</sup>C<sub>3</sub>H<sup>+</sup>, <sup>41</sup>C<sub>3</sub>H<sub>5</sub><sup>+</sup>, <sup>43</sup>C<sub>3</sub>H<sub>3</sub>O<sup>+</sup>, etc.). These peaks are on nearly 100% of the particles in this type. In the negative spectrum the most intense peak is sulfate (<sup>97</sup>HSO<sub>4</sub><sup>-</sup>) and over 95% of these particles have a peak area above 20,000. These particles also have sulfuric acid (<sup>195</sup>H<sub>2</sub>SO<sub>4</sub>HSO<sub>4</sub><sup>-</sup>) on ~80% of the particles, which is even more striking when the transmission efficiency of ~49% at m/z 200 for the co-axial ATOFMS is considered (80). It should be noted that the intensity of the sulfate peak led to considerable ringing, which is seen by the continuum of lower intensity peaks between m/z -98 to -110.

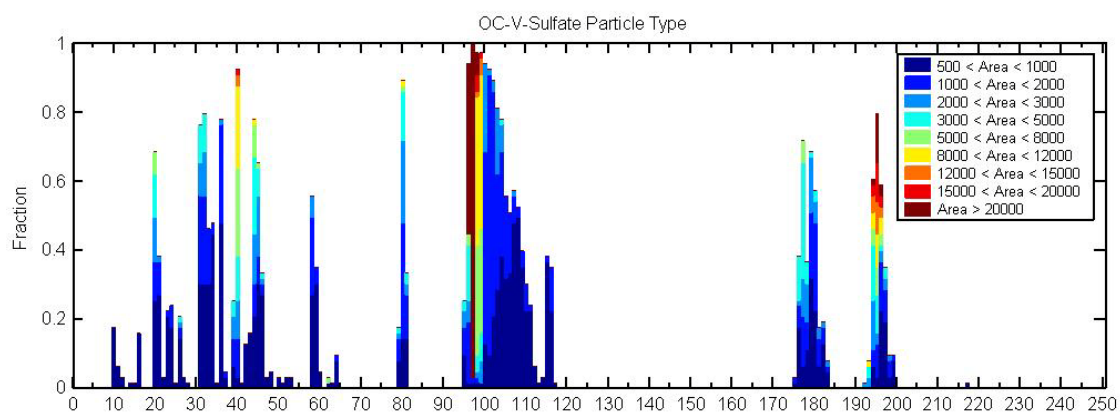
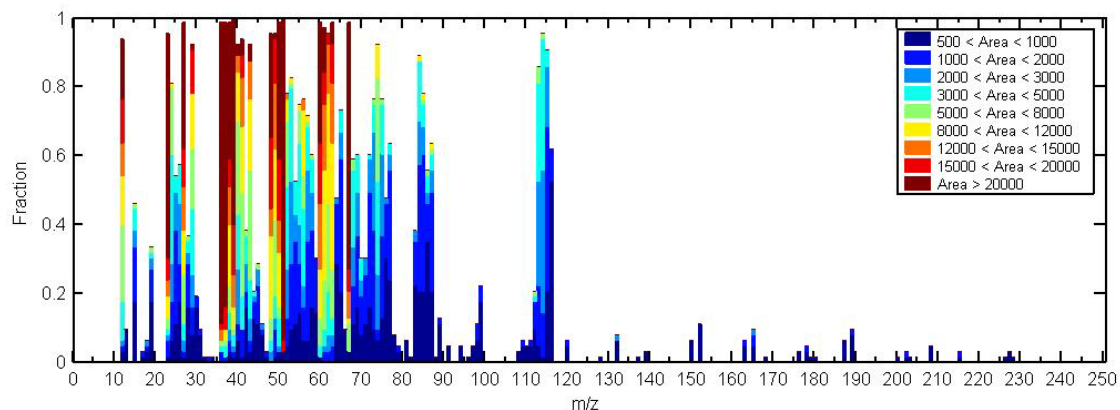


**Figure 11:** A digital color stack for the OC-V-sulfate particle type showing the fraction of particles containing a specific peak on the y-axis versus mass-to-charge on the x-axis. The color represents the fraction containing a specific range of peak areas, with 500 being the lower peak area cutoff. The top portion of the figure represents the positive mass spectrum and the bottom portion represents the negative mass spectrum.

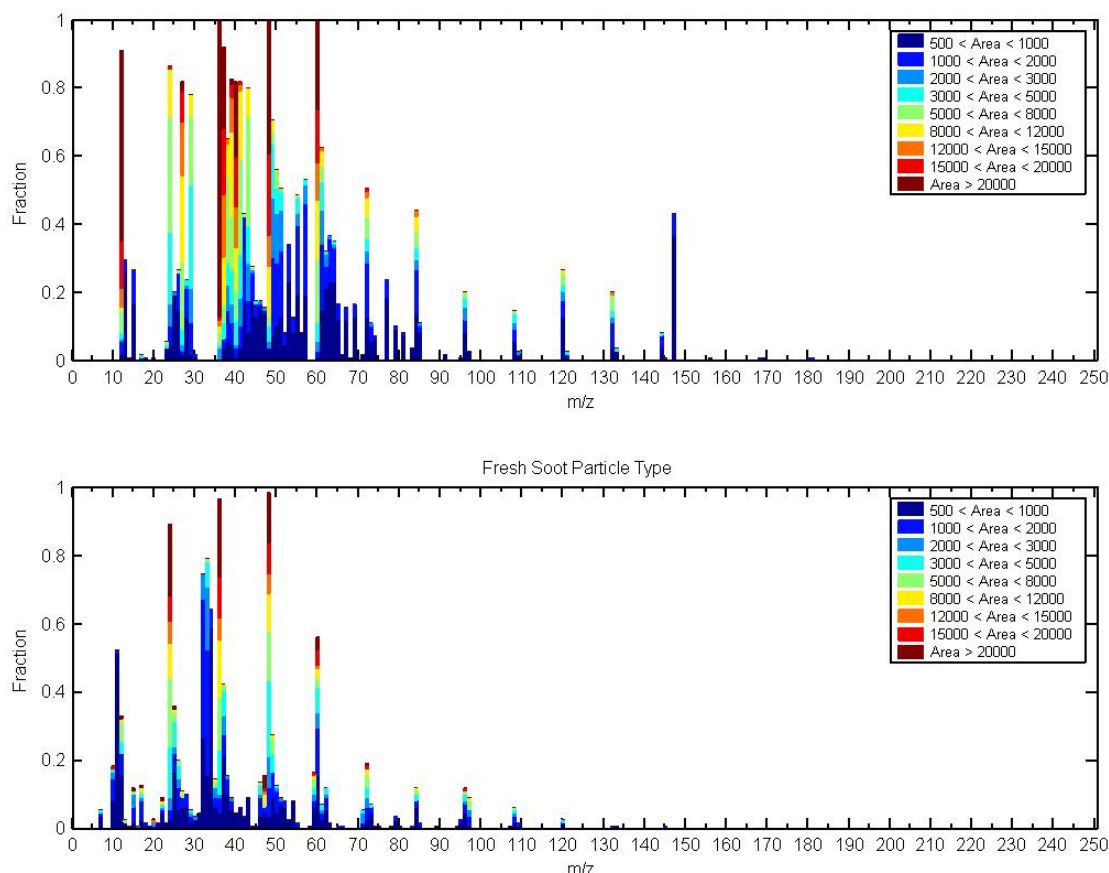


**Figure 12:** A digital color stack for the fresh soot particle type showing the fraction of particles containing a specific peak on the y-axis versus mass-to-charge on the x-axis. The color represents the fraction containing a specific range of peak areas, with 500 being the lower peak area cutoff. The top portion of the figure represents the positive mass spectrum and the bottom portion represents the negative mass spectrum.

The digital color stack for the fresh soot particle type is shown in **Figure 11**, with the same thresholds and range used in **Figure 11**. For Figure S2, intense peaks are observed at mass-to-charges corresponding to carbon clusters ( $^{12}\text{C}^+$ ,  $^{36}\text{C}_3^+$ ,  $^{48}\text{C}_4^+$ , ...,  $^{144}\text{C}_{12}^+$ ) in the positive plot (top). The negative (bottom) plot also shows a similar pattern with respect to the carbon clusters ( $^{24}\text{C}_2^-$ ,  $^{36}\text{C}_3^-$ ,  $^{48}\text{C}_4^-$ , ...,  $^{120}\text{C}_{10}^-$ ). What is notable about the fresh soot type is that < 10% of the particles have a sulfate peak and 0% have a sulfuric acid peak, demonstrating the difference between the two particle types produced in different plumes.

#### *f. Description of the Ca-ECOC Particle Type*

**Figure 13** shows the average mass spectrum of the Ca-ECOC particle type, which is characterized by an intense calcium ion peak ( $^{40}\text{Ca}^+$ ) and elemental carbon clusters in both the positive ( $^{12}\text{C}_1^+$ ,  $^{24}\text{C}_2^+$ , ...,  $\text{C}_n^+$ ) and negative spectra ( $^{12}\text{C}_1^-$ ,  $^{24}\text{C}_2^-$ , ...,  $\text{C}_n^-$ ). The significance of this particle type is that it is enhanced by number along with the fresh soot particle type in distillate fuel plumes. Previous studies have shown higher calcium mass

fractions in filter measurements from the stacks of ships burning distillate fuel compared to residual fuel (61,79).

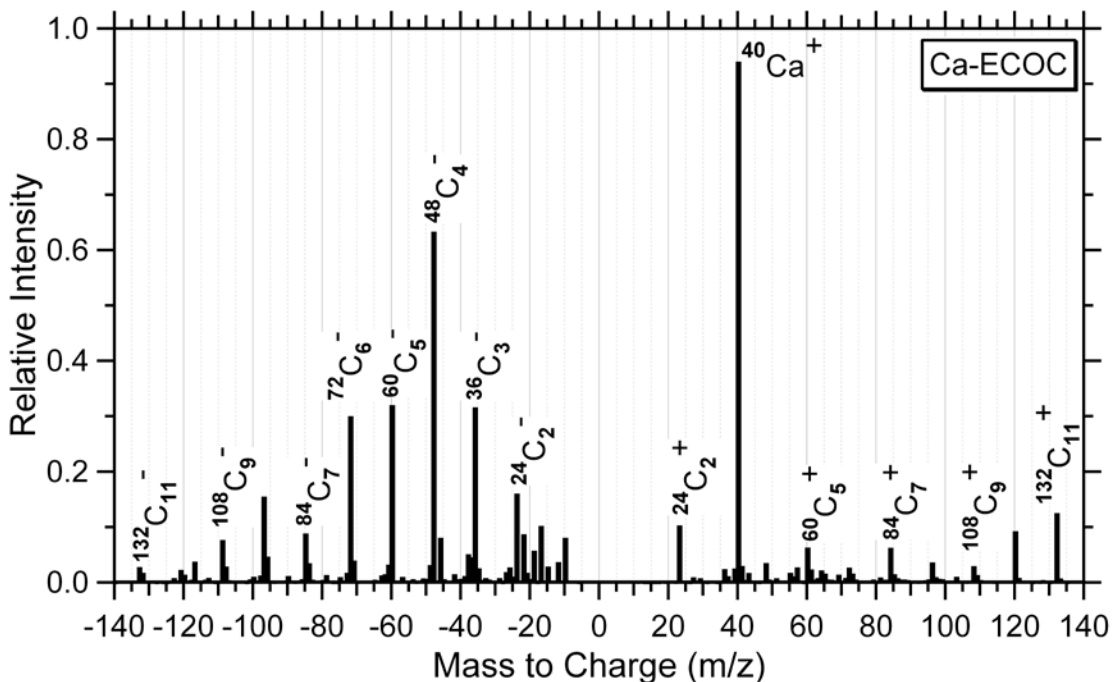


Figure 13: Average mass spectrum of the Ca-ECOC particle type from a fresh soot plume.

### ***g. Background Particle Types During Plumes***

**Figure 14** and **Figure 15** show average mass spectra for the background particle types measured in the plumes from Container1b and Container4. The mass spectra of aged soot particles (**Figure 14a** and **Figure 15b**) were characterized by elemental carbon cluster ions ( $^{12}\text{C}_1^+$ ,  $^{24}\text{C}_2^+$ , ...,  $\text{C}_n^+$ ) with less intense organic carbon markers ( $^{27}\text{C}_2\text{H}_3^+$ ,  $^{29}\text{C}_2\text{H}_5^+$ ,  $^{37}\text{C}_3\text{H}^+$ , and  $^{43}\text{C}_2\text{H}_3\text{O}^+$ ) (81) and secondary markers for sulfate ( $^{97}\text{HSO}_4^-$ ) and nitrate ( $^{62}\text{NO}_3^-$ ). The biomass burning particle type is shown in **Figure 14b** and **Figure 15** and is characterized by a dominant potassium ion peak ( $^{39}\text{K}^+$ ) with less intense elemental carbon markers ( $^{12}\text{C}_1^+$ ,  $^{24}\text{C}_2^+$ , ...,  $\text{C}_n^+$ ) and organic carbon markers  $^{27}\text{C}_2\text{H}_3^+$ ,  $^{29}\text{C}_2\text{H}_5^+$ ,  $^{37}\text{C}_3\text{H}^+$ , and  $^{43}\text{C}_2\text{H}_3\text{O}^+$  (81). The mass spectra of the V-background particle type (**Figure 14c** and **Figure 15c**) are characterized by intense peaks at  $^{51}\text{V}^+$  and  $^{67}\text{VO}^+$  with less intense iron ( $^{56}\text{Fe}^+$ ) and nickel ( $^{58,60}\text{Ni}^+$ ) ion peaks. Note the lack of peaks (other than detector crosstalk) in the negative spectrum which is commonly observed after particles undergo aging and take up significant amounts of water, leading to negative ion suppression (82). These particles have been shown in other marine environments and are likely highly aged (74). Although they share a strong vanadium signal, the temporal trend of the V-background particles did not correlate with those of the freshly emitted OC-V-sulfate particles.

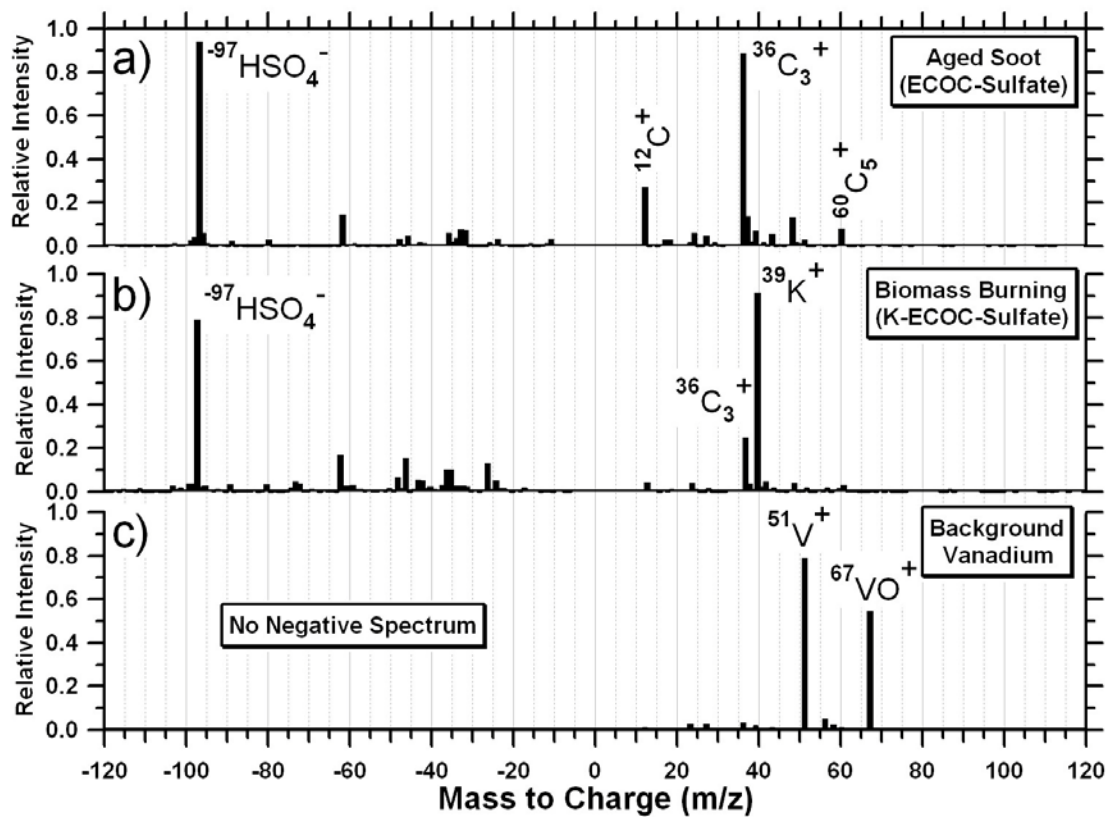


Figure 14: Average mass spectra of background particle types before and after the plume from Container1a.

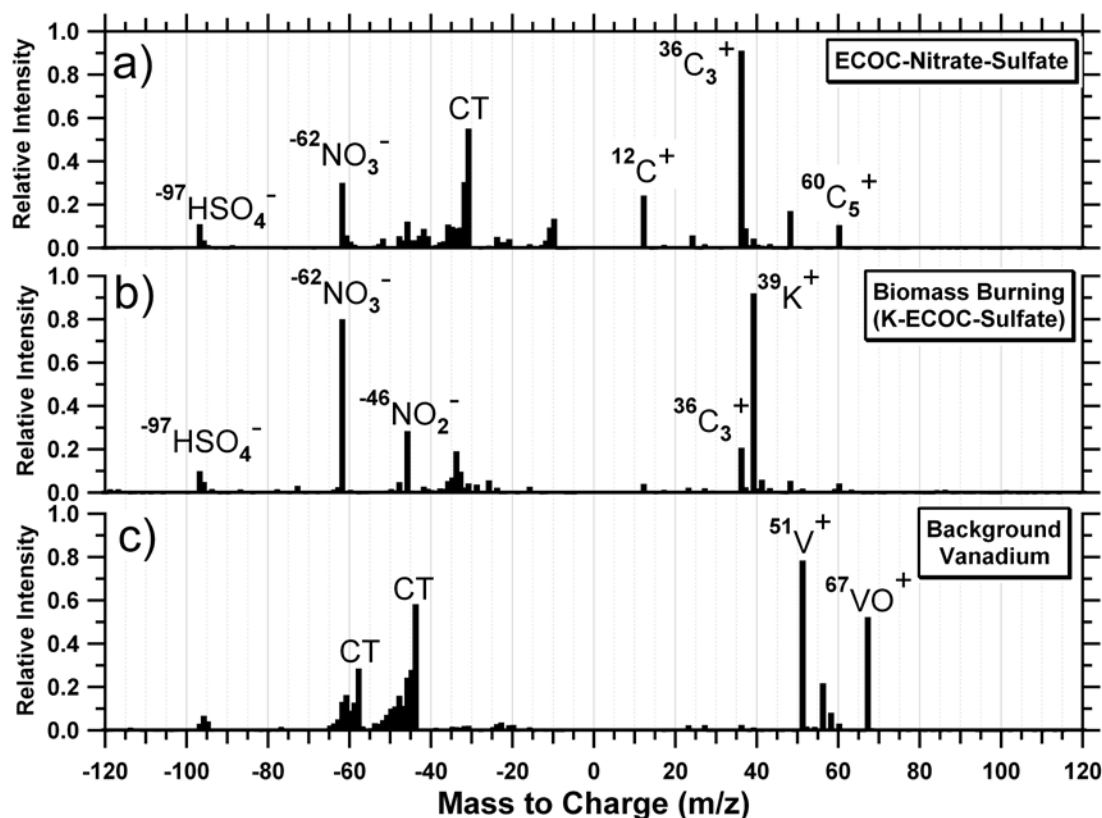


Figure 15: Average mass spectra of background particle types from before and after the plume from Container4. CT represents crosstalk on the detector.

#### *h. Temporal Trends*

**Figure 16** shows the time series of the number of OC-V-sulfate (**Figure 16a**) and fresh soot particles (**Figure 16b**) analyzed by the UF-ATOFMS for the first 5 days of the study. After this period, Santa Ana winds disrupted normal wind patterns. Both time series are characterized by spikes lasting 5-20 minutes. However, as shown in **Figure 16**, OC-V-sulfate and fresh soot spikes frequently spike at different times. Over 65% of the spikes in OC-V-sulfate particles could be correlated to specific ships. Only 15% of the fresh soot spikes corresponded to specific ships, which is understandable as fresh soot is a more ubiquitous particle type associated with many distillate fuel combustion sources including trucks and tug boats (83). Some OC-V-sulfate plumes contained significant fresh soot, while others did not, suggesting that the varying amount of fresh soot in residual fuel combustion plumes may be due to different plume dynamics, engine type and condition, operating conditions, as well as background levels and other emission sources.

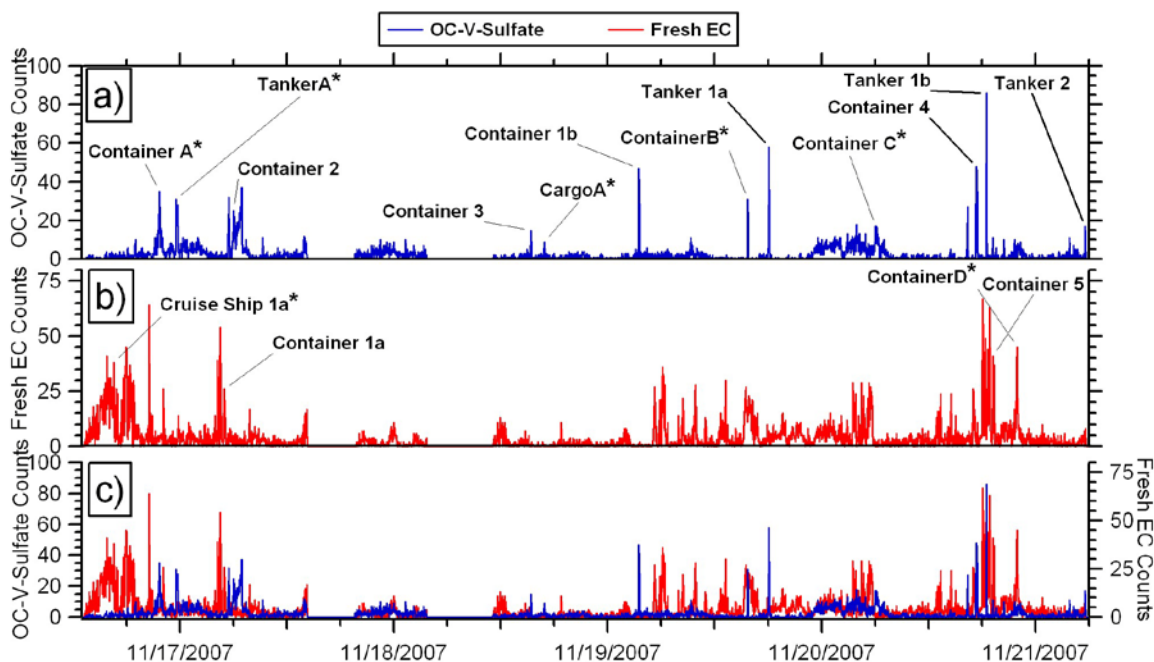


Figure 16: Time series of the differential counting rate (number of ATOFMS counts per 2 minutes) for the OC-V-sulfate and fresh soot particle types. Peaks that could be correlated with ships are labeled; plumes with asterisks were only tentatively identified.

### *i. Size-resolved Chemistry*

The chemical composition with respect to aerodynamic diameter for the urban background before and after both ship plume types is shown in **Figure 17a** (residual fuel combustion plume) and **Figure 17b** (distillate combustion plume). This background is defined as 10 minutes before the plume was detected until 10 minutes after the plume disappeared with the plume itself subtracted out. The particle types associated with the background urban aerosol, in addition to the OC-V-sulfate and fresh soot types, were aged soot, biomass burning, and a background vanadium type. These background particle types did not exhibit a temporal pattern similar to the OC-V-sulfate or fresh soot types, suggesting that they were not associated with the freshly emitted ship plumes.

**Figure 17c** and **Figure 17d** show the particle size-resolved chemical composition for specific ship plumes corresponding to an OC-V-sulfate plume (Container4) and a fresh soot plume (Container1a), respectively. The OC-V-sulfate particles in the residual fuel combustion plume increased 10-25 times in less than 2 minutes from a nearly negligible background level when the plume arrived (**Figure 17a**) to accounting for 28% of 150-500 nm particles (**Figure 17c**). While the UF-ATOFMS was unable to chemically characterize <100 nm particles, measurements of residual fuel combustion exhaust particles using transmission electron microscopy with energy dispersive x-ray spectroscopy have detected distinct peaks of sulfur and vanadium within particles between 30-100 nm in diameter (70). Thus, it is likely that the OC-V-sulfate particle type also represents a significant fraction of even smaller particles emitted in residual fuel combustion exhaust.



For the soot plume (Container1a) a unique mode was observed between 100 – 200 nm composed of fresh soot and Ca-ECOC particles. This differs from the majority of the study when the particle size with the highest detection efficiency was ~ 270 nm due to the combination of inlet transmission efficiencies and ambient concentrations (80), also shown in **Figure 17a**, **Figure 17b**, and **Figure 17c**. However, during the fresh soot plume this was not the case as particles with large geometric diameters (increasing their scattering signal), but small vacuum aerodynamic diameters (100 – 200 nm), were observed. Previous ATOFMS studies measuring particle optical properties have shown that these particles were non-spherical, fractal agglomerates, typical of fresh soot (84). This is supported by previous tandem measurements using a differential mobility analyzer in line with an ATOFMS, showing fresh soot particles having small aerodynamic diameters relative to their geometric diameters indicative of low effective density, fractal particles. (48).

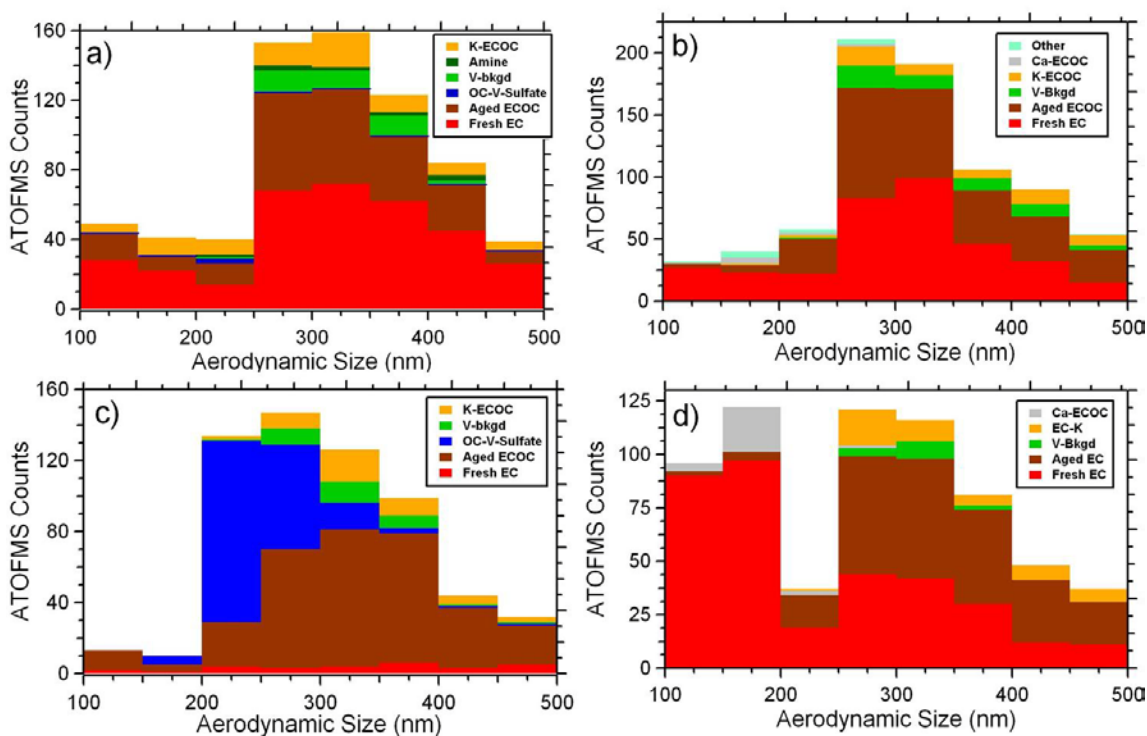


Figure 17: Size-resolved number fractions of the different particle types for the background before and after a) OC-V-sulfate (Container4) and b) fresh soot (Container1a) plumes. (c,d) Size-resolved chemical fractions of these plumes.

#### *j. Correlation between sulfate and vanadium particle*

Rising sulfate levels are a major concern globally (60) and have been shown to influence ship tracks (59). In a representative OC-V-sulfate plume, high fractions of OC-V-sulfate particles contained sulfate (100%) and sulfuric acid (56%), with average absolute peak areas of ~57,000 and 7,000 for sulfate and sulfuric acid, respectively (**Figure 18**). For other particle types only 14-40% of the particles contained sulfate, while almost none (0-1%) contained sulfuric acid. Average absolute peak areas on the other



particle types ranged from only 75-3400 and 0-344 for sulfate and sulfuric acid, respectively. Since ATOFMS absolute peak areas are proportional to mass on a single-particle basis (85,86), differences in the sulfate and sulfuric acid peak areas of ~1-2 orders of magnitude clearly show that the OC-V-sulfate particles contained more sulfate and sulfuric acid compared to non vanadium-containing particles. The measured sulfate and sulfuric acid peak areas are substantially larger than previously measured in ATOFMS source combustion studies, including cars burning gasoline (36), trucks burning diesel (37), and biomass burning (87).

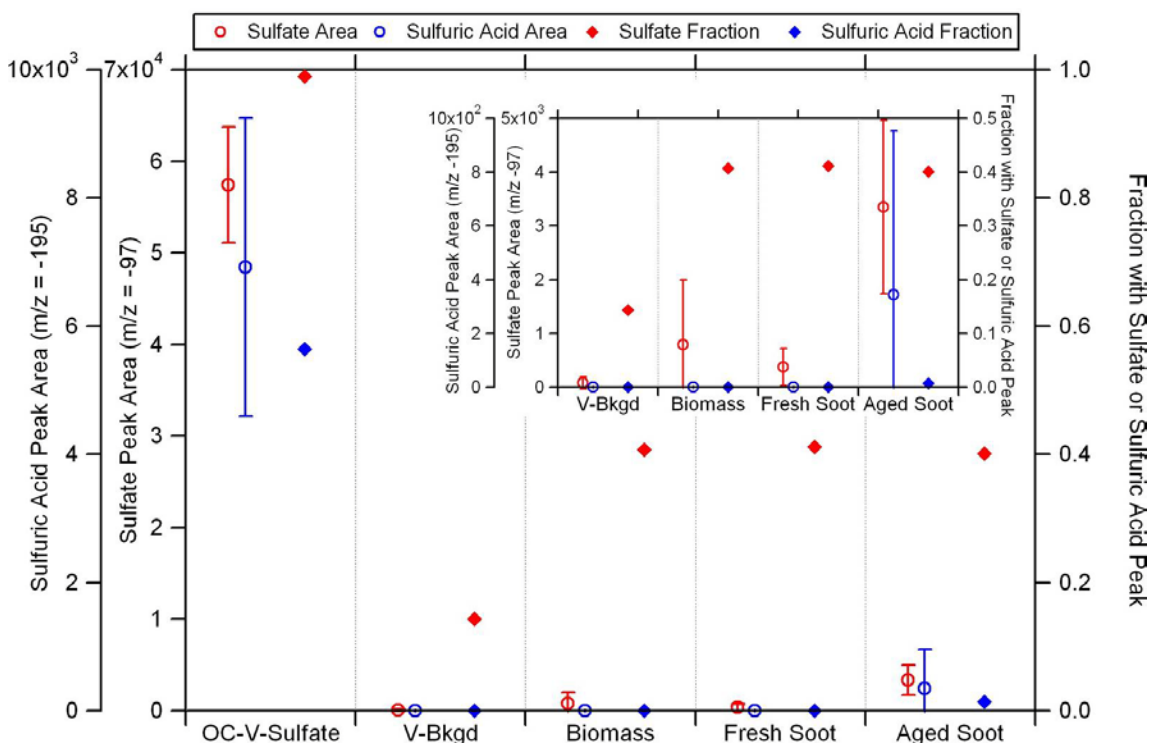


Figure 18: Average sulfate (red circles) and sulfuric acid (blue circles) absolute peak areas for major particle types during the plume of the vessel Container4; errors are shown by 95% confidence intervals. Number fractions of particles containing sulfate (red diamond) and sulfuric acid (blue diamond) are shown. The inset shows a zoomed-in version of particle types with lower peak areas than the OC-V-sulfate type.

There are several mechanisms that could lead to the high measured levels of sulfate in the particle phase of the plume: 1) homogeneous formation of sulfuric acid in the gas phase followed by condensation onto particles, 2) heterogeneous production of sulfate and sulfuric acid on the surface of particles, and 3) aqueous phase production within particles. The gas phase process is too slow to explain our observations of large amounts of sulfate and sulfuric acid forming within minutes of emission (88). This is supported by a study showing that at high relative humidity, aqueous processing is the main oxidation pathway (89). Also, if sulfuric acid was produced in the gas phase, it would condense on all particle surfaces present and lead to sulfate and sulfuric acid on all particle types, not selectively on one type (OC-V-sulfate) as we observe in this study. Thus, the heterogeneous and aqueous phase oxidation of SO<sub>2</sub> to sulfate and sulfuric acid

are the most likely routes. The stronger association of sulfate and sulfuric acid on V-containing particles further suggests the metal(s) are catalyzing this process. Vanadium could be catalyzing the oxidation process (90) or serving as a proxy for other metals present in residual fuel (i.e. Fe and Mn), which the UF-ATOFMS is not as sensitive to as vanadium, that are catalyzing the oxidation process (88).  $V_2O_5$  was originally considered to be ineffective as an atmospheric catalyst below 150 °C (91), but subsequent work has shown that in the presence of  $NO_2$  and adsorbed  $H_2O$ , catalysis of  $SO_2$  by  $V_2O_5$  can occur down to ambient temperatures (25°C) (90). Combine the fact that plumes quickly cool to ambient temperatures (92), that there was high relative humidity in the marine sampling location, and the presence of  $NO_2$  (from the fast reaction between  $O_3$  and  $NO$ ) in the plumes, these atmospheric measurements show that catalytic sulfate production could indeed be an important atmospheric process. Recent work involving oxidation of other sulfur species by vanadium in the laboratory at temperatures between 80-280°C and in the atmosphere show the importance of the catalytic pathway for sulfate production (93,94).

Particulate emissions from ships must be considered as ship emissions are expected to increase ~5% globally by 2030. The production of large amounts of sulfate will impact climate through both cloud and radiative transfer processes (63). Increasing ship emissions will increase concentrations of submicron vanadium-containing particles (61), posing serious consequences for human health (64,65). Herein, direct single-particle measurements of ship plume particle mixing-states provide key insight into the chemistry of freshly emitted ship plumes. The ability to use vanadium as a tracer for ship plumes through single-particle mass spectrometry in the polluted environment of the Port of LA will strengthen efforts to accurately apportion particulate matter to source in other California environments. In addition, current emissions inventories do not account for fuel type and subsequent processing of sulfur species by vanadium and/or other metals (i.e. Fe and Mn) present in the plumes, which could be leading to incorrect estimates of atmospheric sulfate concentrations. Incorporating fuel type could help explain the enhanced sulfate levels being measured in places such as California that current emissions inventories cannot explain (95). Thus, the enrichment of sulfate and sulfuric acid on OC-V-sulfate particles due to catalytic aqueous phase reactions occurring on particle surfaces enriched with vanadium has important implications for regulating anthropogenic sulfate levels in coastal environments. The vanadium and sulfur content of fuels and subsequent impacts on sulfate production should be considered in future inventories and atmospheric models.

#### **iv. Acknowledgements**

The authors acknowledge Dr. Robert Moision and Melanie Zauscher for assistance during the study. Prof. V. Ramanathan and Dr. Craig Corrigan are acknowledged for providing an aethalometer. The Southern California Marine Institute, specifically Dr. Richard Peiper and Carrie Wolfe, hosted the sampling. Funding was provided by the California Air Resources Board (#04-336).